UNIVERSITY
OF OSLO

Master's thesis

Copper based oxides for tandem solar cells

Nicolle Tello Díaz

Physics
60 ECTS study points

Department of Physics
Faculty of Mathematics and Natural Sciences

Spring 2025

Nicolle Tello Díaz

Copper based oxides for tandem solar cells

Supervisors:
Eduard Monakhov
David Rivas
Andrej Kuznetsov

Abstract

Solar energy is one of the most viable replacements for the fossile energy sources due to its availability and status as a well-known sustainable energy source. Searching for materials that can work in tandem configuration with silicon, a material widely used in solar cells, while balancing performance with environmental considerations is an attractive approach. Thus, in this work, we have researched copper-based oxides as compelling candidates for new materials in tandem solar cells.

Reactive magnetron sputtering thin film deposition was used to syntetize copper-zinc-oxide films $Cu_xZn_{1-x}O$ on fused silica substrates, with x varied from 0 to 1. Parameters such as the partial oxygen pressure, deposition temperature, and type of power supply were tested. The effect of these deposition parameters and heat treatment on the structural and optical properties of the samples was studied by X-Ray Diffraction (XRD) and Ultraviolet-Visible Spectroscopy (UV-vis). XRD measurements have demonstrated that depending on the deposition parameters, copper-oxides can be grown as cuprous (Cu_2O) or cupric (CuO) oxide. Post-deposition annealing at 400 °C in air can convert Cu_2O to CuO and improve crystallinity. The growth of ZnO appears to be more stable with respect to the deposition conditions. ZnO films demonstrate significant orientation preference for the c-axis to grow normally to the surface. Changing the deposition temperature can affect this preferential orientation, promoting the (103) orientation. UV-vis was used to determine the band gap of the different samples, indicating that band gap values can be tuned by varying the copper to zinc ratio according to the composition x. We estimate that a band gap of 1.7 eV can be achieved at x around 0.5

Contents

List of Figures

List of Tables

Acronyms

e-beam	electron beam. 35, 36
EDS	Energy Dispersive Spectroscopy. vi, 27, 36, 37, 41, 43, 50
GIXRD	Grazing Incidence X-ray Diffraction. 34, 35
HIPIMS	High-Power Impulse Magnetron Sputtering. 29
PV	Photovoltaic. v, 1, 2, 4–6
PVD	Physical Vapor Deposition. 27
SEM	Scanning Electron Microscopy. vi, 27, 35–37
SIMS	Secondary-Ion Mass Spectroscopy. 28
UiO	Universitet i Oslo. vi, 35, 39
UV-vis	Ultraviolet-Visible Spectroscopy. i, 27, 31, 41, 49, 59, 61
XRD	X-Ray Diffraction. i, vi, vii, 27, 33, 34, 41, 47–51, 53, 59, 61, 62

Aknowledgements

First, I would like to thank my supervisor, Prof. Eduard Monakhov, for his patience and guidance during the development of this work. I would also like to thank my co-supervisor, David Rivas Gongora, for his help and contributions.

I am very grateful to the NORPART project for enabling me to pursue my master's degree in Norway at UiO, especially to those in charge, Andrej and David. I sincerely appreciate their support.

Furthermore, I would like to thank everyone at MiNaLab who helped me understand the workings of the various machines and solve different problems. Eirini, Viktor, Vegard, and Ed have made my life significantly easier. I would also like to express my gratitude to everyone at LENS for making me feel welcome and for enhancing my time in Norway. To all the wonderful friends I made along the way, thank you so much.

Lastly, I want to thank my mom and dad for never doubting my abilities. Their trust in me drives me forward.

Disclaimer on the Use of Artificial Intelligence

The author acknowledges that AI was used for revising and formatting text sections, ensuring grammatical accuracy, and optimizing readability. However, the content, analysis, and conclusions presented within this thesis remain the original work and intellectual property of the author, and any ideas or conclusions derived from these AI-assisted interactions reflect the author's personal insights and academic investigation.

By acknowledging the use of AI in the writing process, the author strives to maintain transparency regarding the methods employed to produce the thesis while ensuring adherence to academic standards set forth by the institution.

Chapter 1

Introduction

Conventional energy sources, such as fossil fuels, coal, and natural gas, have a limited supply and pose significant environmental hazards, including air and water pollution. Consequently, there has been a growing interest in researching renewable energy sources. Among these, solar energy has proven to be one of the most viable replacements due to its worldwide availability, making it a highly sought-after option for sustainable energy solutions [9, 10]. This is where solar cells, or Photovoltaic (PV) cells, come into play, as they are one of the most efficient ways to convert sunlight into electricity.

In order to develop a PV cell, the choice of material is one of the most important factors to consider. This material must be capable of absorbing light and connecting to an external circuit to transfer the generated energy. It generates charge carriers by absorbing photons from the light, which are then guided through the circuit to produce an electric current [11]. The photocurrent generated is proportional to the intensity of the incident light, but the efficiency depends on many factors, including and highlighting the material from which the cell is made.

Considering the need for new materials that strike a balance between cost, performance, and environmental considerations, a tandem solar cell combining silicon (Si) with metal oxides such as copper oxide (CuO) is a rather attractive concept. On one hand, Si is a highly studied and well-known material for solar cells, with a performance quite close to its theoretical limit [12]. On the other hand, copper-based oxides are low-cost, non-polluting, non-toxic, abundant, and exhibit excellent stability in outdoor environments [13, 14], making them compelling candidates for research as new materials for tandem solar cells.

1.1 Solar Cells: A brief history

Given the importance of solar cells for the future of renewable energy, a brief history is useful for understanding how we have reached this point.

The foundation of solar cell technology lies in the discovery of the photovoltaic effect. In 1839, Edmond Becquerel placed two electrodes in an acidic solution and observed that exposing one of them to light generated an electric current [15]. However, it would take many more years before the mechanisms behind the photovoltaic effect were fully understood.

After that, in 1876, William Adams and Richard Day [16] made the first solid state PV device after discovering that selenium produces a current when exposed to light. A few years later, Charles Fritts [17] developed the first large-area solar cell by pressing a layer of selenium between gold and another metal, however, this cell had an efficiency of just 1%.

The mechanism behind the photovoltaic effect was not understood until 1914, when Goldman and Brodsky related the existence of a potential barrier, or rectifying barrier, in the metal-semiconductor junction to the effect. This theory was further developed by Walter Schottky, Neville Mott, and others [11].

It wasn't until the 1950s, with the introduction of silicon, that we saw the first modern Si solar cell, developed by Darryl Chapin, Calvin Fuller, and Gerald Pearson at Bell Labs. This cell, created in 1954, was the first to generate enough current to power everyday electrical devices, even though it only had an efficiency of 6% [18]. This period also saw increased attention to p-n junctions as rectifying mechanisms, compared to metal-semiconductor junctions. The ability of solar cells to produce sufficient energy for device operation made them particularly valuable in locations where access to the electrical grid was difficult or impossible, such as space, coinciding with the onset of the space race [11].

Years later, in the 1970s, the energy supply crisis led to a significant increase in interest in solar energy as a renewable source. This renewed focus on solar energy spurred improvements in solar cell technology. By the 1990s, the production of solar cells was expanding at a rate of 15-25% per annum [11]. Additionally, there were advancements such as the development of thin-film solar cells, which provided more flexibility in their applications.

After so many advancements, the industry of solar cells nowadays is such that solar energy can now compete with the traditional energy sources, being quite attractive due to all the benefits that it brings in terms of sustainability and general availability worldwide. Figure 1.2 shows the advancements up to 2023, showing the conversion efficiencies of various PV technologies.

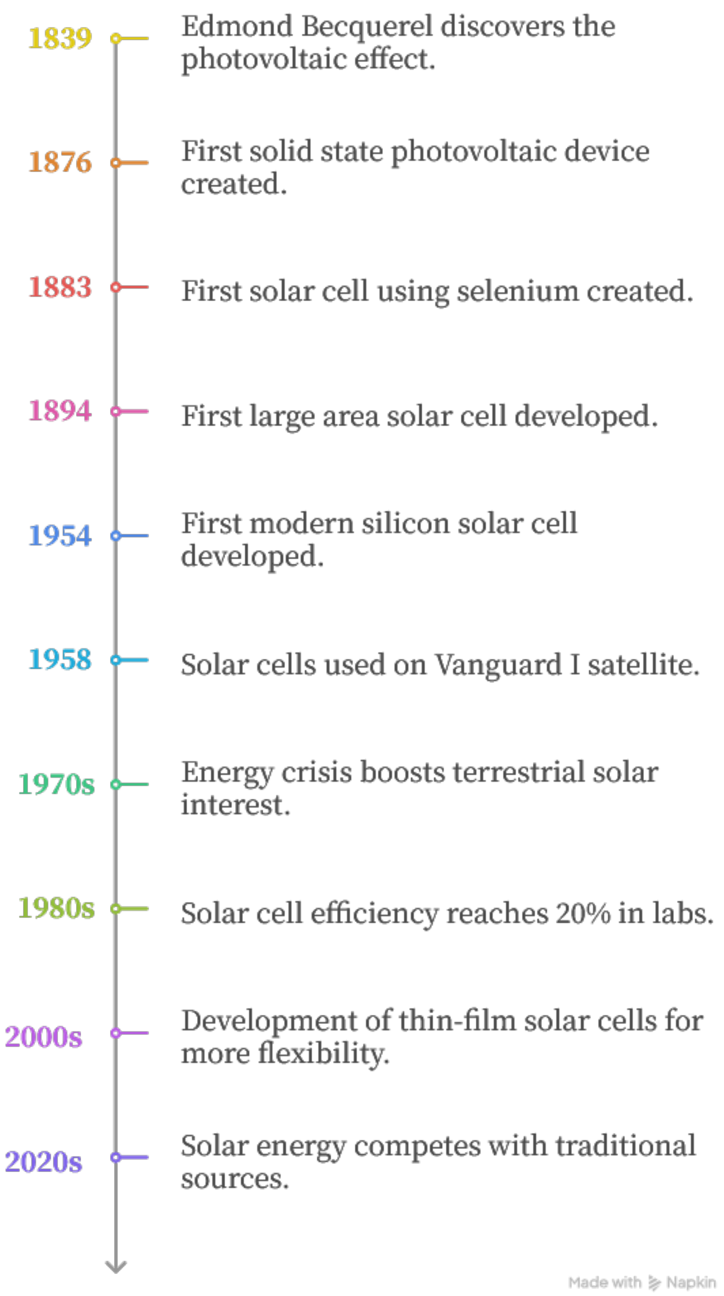

Figure 1.1: Timeline summarizing some of the milestones in the history of the solar cell.

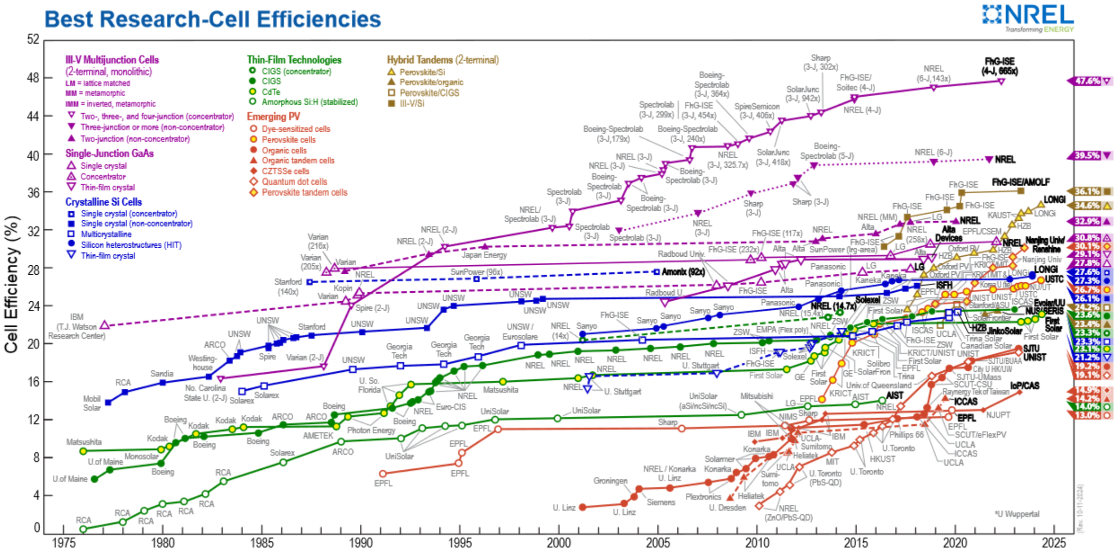

Figure 1.2: Conversion efficiencies of the best solar PV cells from 1976 to 2023 for various PV technologies. This data is tracked by the U.S. Department of Energy's National Renewable Energy Laboratory [19].

1.2 Silicon in Tandem Solar Cells

The importance of silicon in the PV industry is undeniable, as it dominates the market by a significant percentage. According to the International Energy Agency (IEA), as of February 2025, crystalline silicon holds a market share of over 98% [20]. However, as newer cells approach both theoretical and practical efficiency limits, alternative approaches are becoming necessary to enhance efficiency. One such approach involves using tandem or multi-junction cells [21].

Tandem cells involve stacking two solar cells to increase efficiency by absorbing complementary parts of the solar spectrum. Figure 1.3 shows a configuration of the tandem cells with silicon as the bottom cell, the arrows exemplify how part of the spectrum is absorbed by the top cell before reaching the bottom cell. Their operation is further explained in Section 2.2.4.

Given silicon's wide usage in the market, using it as a base for new approaches is

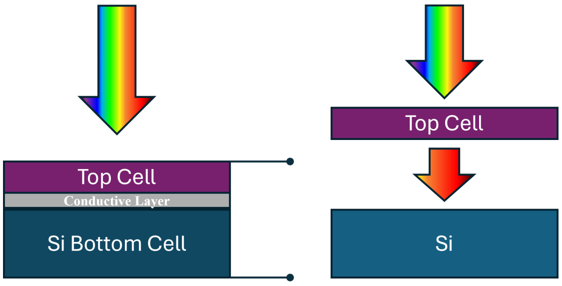

Figure 1.3: Example of a two-terminal coupling for a tandem solar cell with silicon as the bottom cell. The colored arrows are to show how part of the solar spectrum is absorbed by the top cell

logical, as it would reduce costs associated with industry changes. Silicon is well-suited as a bottom cell in a tandem configuration due to its favorable properties for solar cell applications, including abundance, low cost, and extensively researched efficiency improvements. With a band gap of 1.12 eV, silicon is an excellent choice to use in tandem solar cells, and by adding a top cell with a wider band gap, increasing the efficiency of the PV cell is entirely possible. However, selecting the appropriate top cell remains a challenge [21, 22].

Yu, Leilaeioun and Holman [21] conducted a study on the properties of the top cell in silicon-based solar cells by using the detailed-balance model and concluded that the optimal band gap for a top cell in this configuration is 1.7 eV.

1.3 Perovskite Solar Cells

Lead halide perovskite solar cells (PSCs) are part of what is called the third generation, or emerging generation, of solar cell technology. These materials first appeared as a PV alternative to silicon solar cells in 2009, introduced by Kojima et al. [23]. Perovskites refer to any material that shares the crystal structure of calcium titanate, which has the general formula ABX_3, where A and B are cations of different sizes and X is an anion.

They are extensively researched due to their optimal optoelectronic characteristics and reduced production costs compared to other materials, while maintaining high efficiencies [24].

In general, we can summarize their qualities as follows:

- Efficiency and performance:

  These materials have shown great performance and efficiency, now exceeding 22%. However, as there are various methods of fabricating these semiconductor perovskites, there is still room for improvement [25, 26].

- Fabrication:

  These cells can be fabricated through various methods, including deposition from organic solutions at low temperatures, which is time- and cost-effective while maintaining high crystalline and electronic quality [26].

- Tandem use:

  They can be used in tandem configurations with materials such as silicon, enhancing their efficiency and facilitating their implementation in an existing industry [27].

However, despite appearing to be optimal materials for PV devices, they face several major challenges [24–26, 28]:

- Stability and degradation:

  They have been shown to be very unstable under various conditions, such as moisture, heat, and UV radiation, making them unsuitable for normal use. They have yet to demonstrate long-term stability.

- Environmental considerations:

  Their most significant problem is that all high-efficiency PSCs use lead as a major constituent. This, combined with their inadequate stability, poses a substantial threat to both the environment and human health, introducing a toxicity factor during development, use, and disposal.

1.4 Copper-based oxides

As was mentioned before, copper-based oxides are low-cost, non-polluting, non-toxic, abundant, and have shown excellent stability in outdoor environments [13, 14].Therefore, it makes sense to consider them for PV applications.

Copper oxide is a p-type semiconductor that can be present in three different phases: cuprous oxide (Cu_2O), cupric oxide (CuO) and paramelaconite (Cu_4O_3)[29]. The former two, figure 1.4, have been more extensively researched. Among them, Cu_2O has been well studied in the past, both theoretically and experimentally, and with a direct band gap of about 2.17 eV it is a compelling candidate for its use as an absorber in PV cells [29, 30].

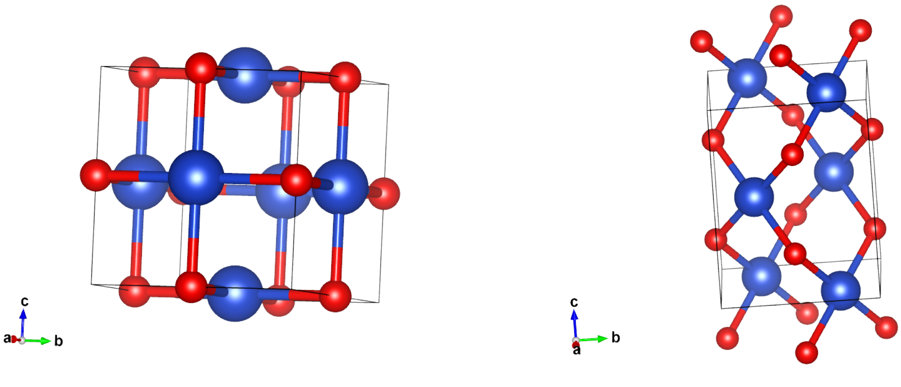

(a) Cu_2O (b) CuO

Figure 1.4: Crystal structure of Cu_2O and CuO, graph using VESTA with the data from Jain et al. [1] and Materials Data on CuO by Materials Project [2].

Cupric oxide (CuO), figure 1.4b, is a p-type semiconductor with a narrow indirect band gap [30]. Although this material has also been studied for PV applications, much remains to be done on this material. Theoretically, determining the band structure of this material has been challenging, and as such, we find various theoretical band gap values for CuO in the literature [31–33], however, experimental data shows values of

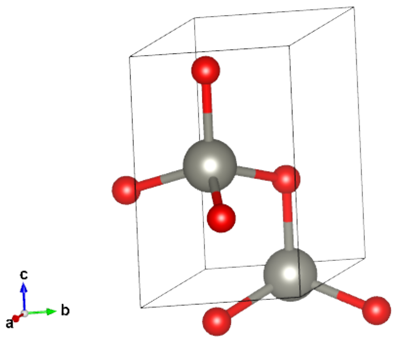

Figure 1.5: Crystal structure of ZnO, graph using VESTA from Materials Data on ZnO by Materials Project [3].

the band gap around 1.4 eV [34, 35], in concordance with the theoretical results of Heinemann, Eifert and Heiliger [30]. Considering what Yu, Leilaeioun and Holman [21] showed, a top cell to be used in tandem configuration with silicon should have a band gap of 1.7 eV, CuO alone is not an ideal partner.

On the other hand, zinc oxide (ZnO) is an n-type semiconductor with a wide direct band gap of around 3.4 eV. Thus, we consider alloying zinc oxide (ZnO) together with cupric oxide (CuO) as a way to tune the band gap towards the optimal value of 1.7 eV. Therefore, in this work, we present the system $Cu_xZn_{1-x}O$, where x is the atomic percentage.

However, some challenges may present themselves, considering the differences in structure and band gap of both materials. This will be addressed during the development of this thesis.

1.5 Aim of the Study

The goal of this project is to develop and analyze potential new materials for solar cells, focusing specifically on copper-based oxides. In particular, the study examines copper-zinc oxides of the form $Cu_xZn_{1-x}O$, where x represents the atomic percentage. We aim to tune the band gap of the material to enhance its properties for application as the top cell in a tandem configuration with silicon.

In particular, we investigate the effect of using different deposition parameters, such as temperature and pressure settings, and heat treatments on both the structure and optical characteristics of the material.

The following chapters of this thesis will further elaborate on the process that was followed:

- Chapter 2 explains the mechanisms that enable solar cells to function, as well as the general behavior of semiconductors.

- Chapter 3 shows the principles of the experimental methods used in the obtention and characterization of the samples.
- Chapter 4 presents all the data gathered from the samples, aiming to explain changes in the structure and photoelectronic properties due to variations in Zn concentration, deposition temperature, and annealing processes.
- Finally, Chapter 5 presents the conclusions reached during the development of this thesis and a brief look into future possibilities.

Chapter 2

Theoretical Background

2.1 Semiconductors: Definition and Properties

The band gap defines what a semiconductor is and explains its behavior. In solid state, each material has a characteristic band structure responsible for its different electrical behaviour. For a material to conduct electricity, electrons must be able to move through it, which means that a transition between different electronic states must occur. If all available states are filled, electrons cannot move, and the material cannot conduct electricity. Such materials are called insulators, where the valence band is filled, leaving no available states for electron movement, and a wide band gap (over 6 eV) makes it difficult for electrons to be excited to higher energy levels in the conduction band [4].

Conversely, metals have overlapping valence and conduction bands, providing plenty of available states for electron movement, making them highly conductive. Metals can also have partially filled bands, allowing easy electron movement throughout the material [4].

Finally, semiconductors - the materials of interest in this project - behave as insulators at 0 K, with a filled valence band and a gap between the valence and conduction bands. However, the band gap in this case is smaller than that of insulators (about 0.5 - 3 eV), enabling electrons to be promoted to the conduction band when excited, such as by thermal excitation or photon absorption, facilitating carriers' movement in both bands [4]. Figure 2.1 illustrates how the band gap differentiates insulators, metals, and semiconductors.

Semiconductors naturally lend themselves to electronic device applications. Their band gap, intermediate between metals and insulators, allows for tunable properties suitable for various applications, adjustable through temperature, optical excitation, doping, or composition. The band gap is crucial for a semiconductor's function as a photovoltaic device, as it determines the material's performance [4, 36]. Hence, understanding semiconductors begins with defining the band gap.

In this Chapter, we will follow the developments of Nelson [11], Streetman and Banerjee [4] to understand the theoretical background behind this project. However,

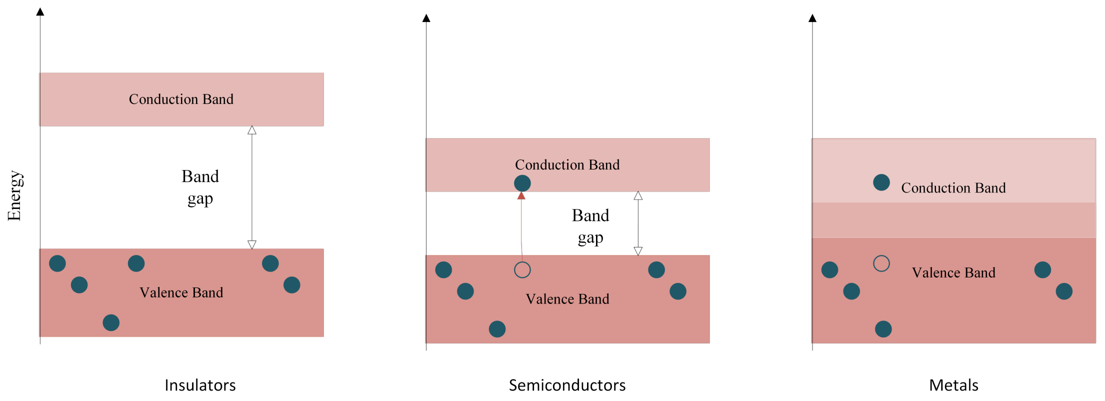

Figure 2.1: Schematic difference between insulators, semiconductors and metals by their band gap.

we will not focus on the mathematical developments but more on understanding the concepts behind them.

2.1.1 The Band Gap

How is it formed?

In atoms, electrons are confined to discrete energy levels defined by atomic orbitals. By considering a system with two electrons centered around two nuclei, the wavefunction of these electrons becomes a linear combination of individual atomic orbitals, resulting in two distinct normal modes:

- Antibonding Orbital: Characterized by an odd or antisymmetric combination, it has higher energy and a lower electron probability density in the region between nuclei.
- Bonding Orbital: Defined by an even or symmetric combination, it has lower energy and a higher electron probability density in the region between nuclei.

In the bonding state, electrons have opposite spins, while in the antibonding state, they have parallel spins, leading to repelling forces [4]. Figure 2.2 illustrates this, showing a bonding energy orbital that is lower to that of the antibonding, due to the attraction of the electrons from both nuclei. Conversely, the higher energy levels increase as the nuclei get closer, indicating stronger repulsion.

In solids, a large number of atoms are in proximity, resulting in a range of closely available energies. This allows electrons to move more freely between these energy bands without needing to jump significant distances. The overlap of wavefunctions from electrons of neighboring atoms contributes to this phenomenon, causing electrons not to belong to a single atom [4].

In semiconductors, there is a characteristic gap between the valence and conduction bands. This band gap represents a range of energy values where no electronic states

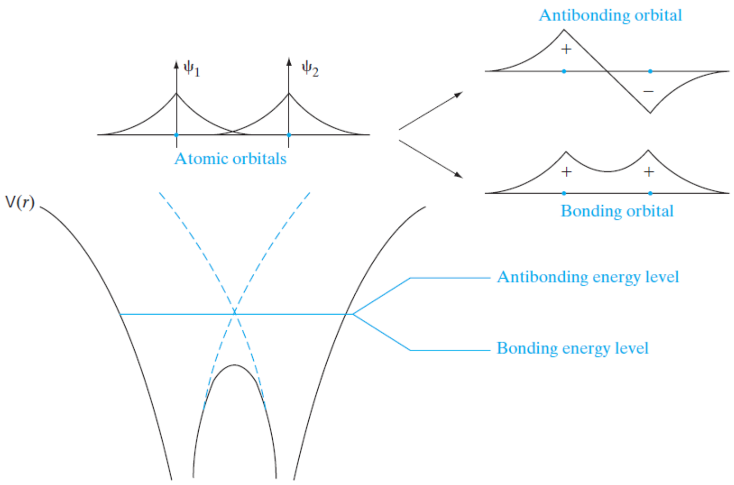

Figure 2.2: Schematic representation of bonding and antibonding atomic orbitals and their overlapping. From Streetman and Banerjee [4]

can exist. To illustrate this, consider carbon or silicon atoms brought together to form crystals: at large interatomic distances, the s and p orbitals are clearly distinguishable, as there is no overlap of the electron wavefunctions. However, as interatomic distances decrease, overlapping occurs, allowing the bands to be continuous and the orbitals to merge. As the atoms come closer together, the repulsion in the antibonding state increases, resulting in a separation of the formed energy bands and the emergence of the band gap. Semiconductor materials have interatomic distances that, in their solid, crystallized state, allow for the presence of a band gap [37, 38]. This is exemplified in the Figure 2.3.

Now we know how the band gap is formed, but we still have the question of why is it important.

The Importance of the Band Gap and How to determine it

The band gap not only distinguishes semiconductors from metals and insulators but also defines the functionality of the semiconductor for various applications. The effectiveness of a semiconductor as a solar absorber material in a photovoltaic (PV) cell is primarily determined by the value of its band gap [36].

The band gap allows excited electrons to remain at higher energy levels long enough to be utilized. In systems with continuous energy levels, excited electrons quickly thermalize back to the lower energy state available. However, when there is a gap between these levels, the probability of rapid thermalization decreases. This provides sufficient time for electrons to be transferred to the rest of the system and used for generating electrical current [11].

Although the band gap is defined due to the absence of electronic states between energy levels, this is not fully true in all real materials. If electronic states are found

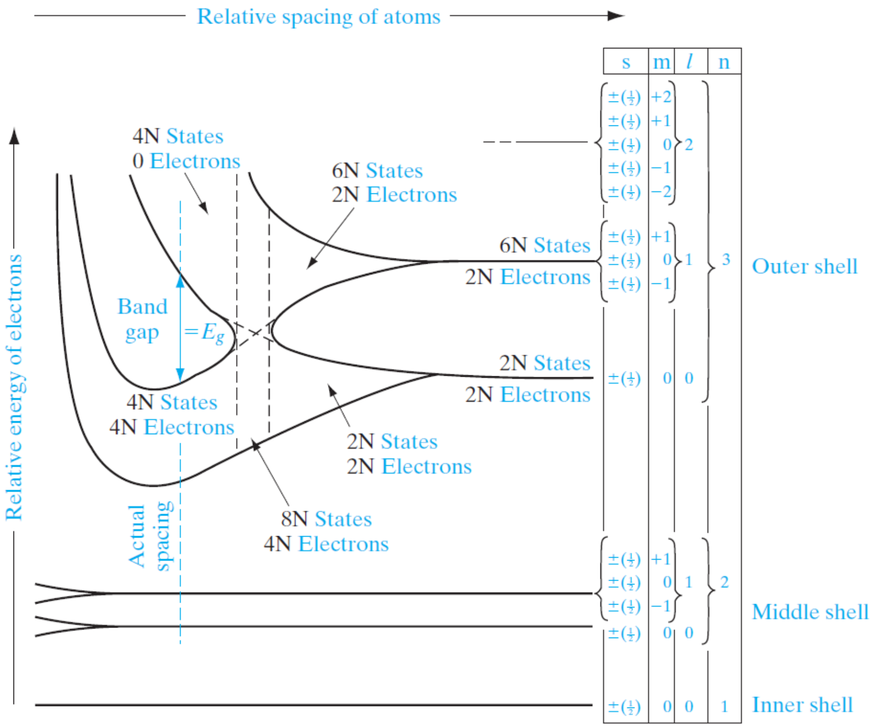

Figure 2.3: Energy levels in silicon as a function of the relative interatomic spacing. From Streetman and Banerjee [4].

within this gap, they can be attributed to defects in the now non-ideal periodic crystal. Thus, in most crystalline materials, a perfect gap and a perfect definition of the band gap cannot exist.

As the band gap requires the existence of well differentiated conduction and valence bands, knowing the band structure of a material is quite usefull to help determine theoretically this property. For this, we need to determine the energy levels of the material, which are obtained by solving the Schrödinger equation. The typical way of calculating it is by considering an electron traveling through a perfectly periodical crystal lattice, so that the wavefunction of the electron is

$$\psi(\mathbf{k},\mathbf{r}) = u_{i\mathbf{k}}(\mathbf{r})e^{i\mathbf{k}\cdot\mathbf{r}}, \tag{2.1}$$

with $\mathbf{k}$ the wavevector, i denotes the crystal band and u is a function that modulates the wavefunction. From solving the Schrödinger equation we can obtain the eigenenergies ($E(\mathbf{k})$) for each crystal band i and for each $\mathbf{k}$. These energies can be plotted against $\mathbf{k}$ in order to get the crystal band structure.

The crystal band structure of a semiconductor would have a minimum energy value in the conduction band and a maximum in the valence band. The transition of a electron from these two points is the smallest-energy transition between the bands, however, if these points do not coincide in their $\mathbf{k}$ value, the transition would require a change in momentum. This allows us to define two types of band gaps: direct and indirect (figure

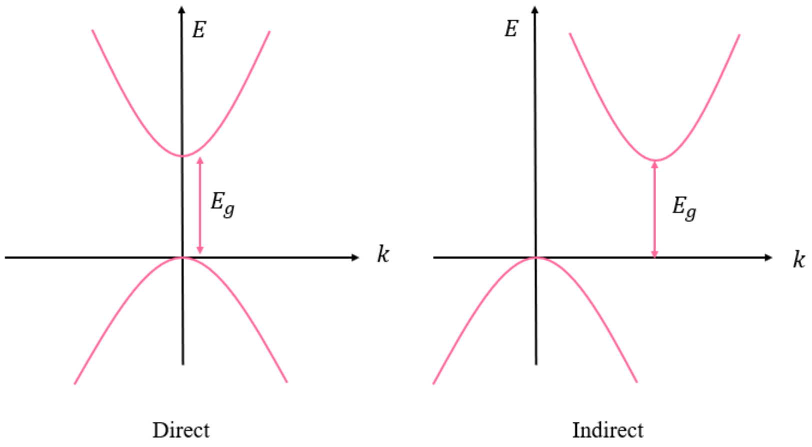

Figure 2.4: Schematic showing the variation of direct and indirect band gap.

2.4), with the former being where the transition does not require changes in **k**.

2.1.2 Electrons & Holes

This section follows the definitions and explanations by Nelson [11].

Band gaps typically arise in materials where all of the valence electrons participate in bonding, aiming to minimize energy. At absolute zero temperature, all valence electrons in a pure semiconductor are involved in bonding and are not free to move. However, as the temperature increases, additional kinetic energy allows the electrons to break free of the bonds. This makes it easier to excite these electrons to higher energy levels, such as those in the conduction band. Another way, is to have photons excite the valence electrons, which works as long as the light has an energy greater than the band gap.

Electrons that break free and are excited into the conduction band leave behind vacancies known as 'holes'. These holes can move, as they are continuously filled by other valence electrons, allowing them to participate in conduction. Given that the holes left by the excited electrons are considerably fewer than the valence electrons, it is logical to refer to them and the excited electrons when describing the material's conductivity, rather than considering the more numerous valence electrons moving against the field.

Both holes and electrons can be characterized by their mobility (μ_n and μ_p, respectively) and effective mass (m_n^* and m_p^*). These are referred to as charge carriers, or simply carriers, and their concentration is fundamental for characterizing semiconductors.

2.1.3 Doping

Doping consist in introducing impurities in a material in order to change its electrical properties. As this impurities change the charge carrier concentration, it is important to understand how this values are obtained and the distribution of these charge carriers over the available states. First, we should describe an intrinsic semiconductor.

An intrinsic semiconductor can be described as a perfect crystal with no impurities. At a temperature of 0 K, electrons fill the energy levels starting from the lowest one available, so that the highest energy level filled by electrons at this temperature is the Fermi energy level (E_F). At higher temperatures, electrons gain kinetic energy and can be excited to levels above the Fermi level. In an intrinsic semiconductor at absolute zero, the valence band is completely filled, while the conduction band remains empty, placing E_F within the band gap.

Another essential concept for understanding intrinsic semiconductors is the intrinsic energy (E_i), which is the Fermi energy level in an intrinsic semiconductor. Similarly, the intrinsic carrier concentration is defined as the charge carrier concentration for an intrinsic or perfect semiconductor and it is the same for both electrons in the conduction band (n_i) and holes in the valence band (p_i), as they are created in pairs for an intrinsic semiconductor:

$$p_i = n_i. \tag{2.2}$$

In general, electrons in solids follow Fermi-Dirac Statistics, meaning that, by considering their wave nature, the Pauli exclusion principle and their indistinguishability, one can determine the distribution of electrons at thermal equilibrium as

$$f(E) = \frac{1}{1 + e^{(E-E_F)/kT}}, \tag{2.3}$$

where k is the Boltzmann constant and T is the temperature. This Fermi-Dirac distribution can be used to determine the concentration electrons in equilibrium in the conduction band as

$$n_0 = \int_{E_c}^{\infty} f(E)N(E)dE \tag{2.4}$$

$$n_0 = N_c e^{-(E_c-E_F)/kT}, \tag{2.5}$$

where $N(E)$ is the density of states and N_c is the effective density of states in the conduction band. Similarly, we can get the expressions for the concentration of holes in equilibrium in the valance band as

$$p_0 = N_v e^{-(E_F-E_v)/kT}, \tag{2.6}$$

with N_v the effective density of states in the valence band. Following this, we can get expressions for the intrinsic carrier concentrations:

$$n_i = N_c e^{-(E_c-E_i)/kT}, \quad p_i = N_v e^{-(E_i-E_v)/kT}. \tag{2.7}$$

Typically, impurities and defects in materials introduce changes and additional bonds to the crystal, affecting the electronic energy levels. These changes are generally localized. The addition of this impurities also makes it so that the equilibrium carrier concentrations differ from the intrinsic carrier concentrations. Thus, we have an extrinsic material.

An interesting phenomenon occurs when impurity energy levels appear within the band gap, influencing the semiconductor's properties. An occupied impurity level above E_i will raise the Fermi level, increasing the electron density compared to holes in equilibrium. Conversely, if the impurity level is below E_i and unoccupied, it would lower the Fermi level, increasing the hole density as electrons can be excited to these unoccupied levels.

The process of increasing the density of either holes or electrons by introducing certain impurities with defined energy levels near the conduction or valence bands is known as doping. Doping can be divided into n-type and p-type, depending on whether the main charge carriers are positive (holes) or negative (electrons). Figure 2.5 shows how the doping works with both p-type and n-type doping.

- n-type doping

  This type of doping works by introducing impurity atoms, called donors and with a concentration N_d, that have one extra valence electron than the number of bonds. We want these impurity levels to be introduced closer to the conduction band E_c, so that the extra electron can be easily donated to the conduction band, increasing the amount of carriers there ($N_d \approx n_0$). Since this increases the electron density over the hole density, electrons are called majority carriers in this case, while holes are minority carriers.

- p-type doping

  This type of doping, on the other hand, works by introducing impurity atoms, called acceptors, that are missing one valence electron than the number of bonds in the lattice, of concentration N_a. In this case, we want these impurity levels to be closer to the valence band E_v, so that they easily accept electrons from the valence band, allowing for holes to move and increasing the conductivity ($N_a \approx p_0$). Here we have that holes are greatly increased compared to electrons, and as such they are called the majority carriers, while electrons are the minority carriers.

2.1.4 Mobility

Mobility is how easy it is for charge carriers to move through a crystal. As charge carriers collide with both the lattice and with impurities, this mobility is dependent on both temperature and impurity concentration.

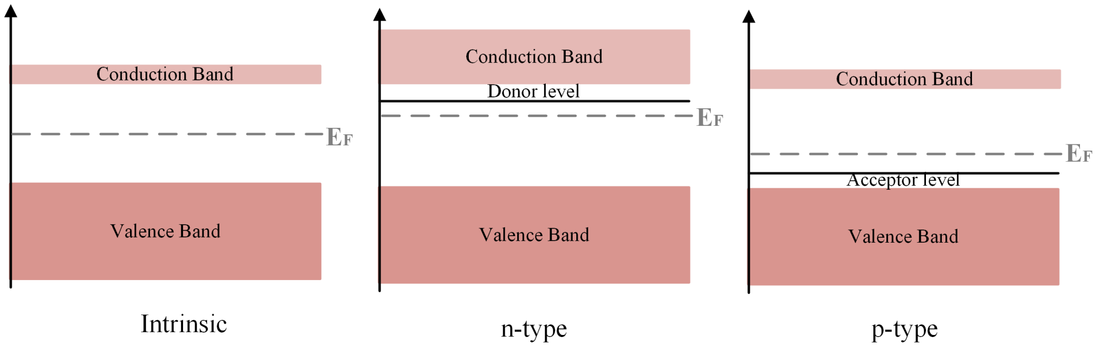

Figure 2.5: Schematic of the effect of the donor and acceptor energy levels on the Fermi energy level. Based on a graph by Streetman and Banerjee [4]

In general, if there is no external force, the movements of the electrons inside the crystal are random and as such they do not show any preferential direction of motion and there would not be any current flow. However, if there is an electric field, although it probably would not fully alter the randomized trajectory of the electron, it would alter the general motion of the electrons, defining the direction of the net motion of the electrons.

To show this, if we consider an electric field applied in the x direction $\mathcal{E}_x$, we would have an average momentum per electron as

$$\langle p_x \rangle = -q\bar{t}\mathcal{E}_x,$$

Which in turn means the electrons have an average velocity of

$$\langle v_x \rangle = \frac{\langle p_x \rangle}{m_n^*} = -\frac{q\bar{t}}{m_n^*}\mathcal{E}_x.$$

Here $\bar{t}$ is the mean free time, or the mean time between scattering events. This net speed does not properly describe the movement of individual electrons due to thermal motions, as this movement is random and in various directions, however, it does show the effect of the electric field in the movement of the electrons. From here we can also get an expression for the electron mobility

$$\mu_n = \frac{q\bar{t}}{m_n^*}.$$

Which shows the ease of the electrons to drift inside the material. From here we can also get the current density in terms of the mobility fo both electrons and holes as

$$J_x = q(n\mu_n + p\mu_p)\mathcal{E}_x$$

Now, mobility can be affected by scattering, from these processes we can highlight lattice scattering, where the carrier is scattered by the vibrations of the lattice and

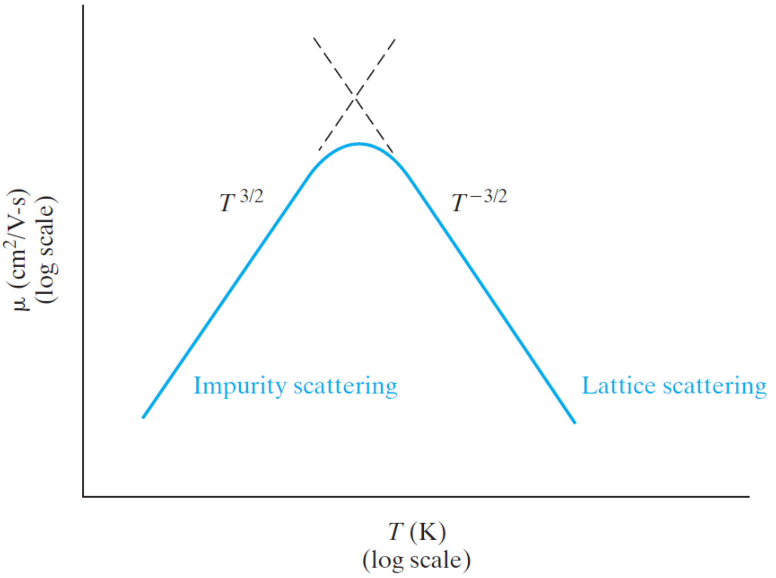

Figure 2.6: Schematic temperature dependence of the mobility μ, showing regions of impurity and lattice scattering. From Streetman and Banerjee [4]

impurity scattering, where the carrier collides with the impurities and as such its mobility is impaired. Both of these events are affected by the temperature, but in opposite ways.

Lattice scattering becomes relevant when the temperature starts increasing the vibrations of the lattice and as such increasing the scattering events due to it. However, in impurity scattering, at lower temperatures the carriers do not have enough momentum to not be affected by the interaction with a charged ion. As such we have that at lower temperatures the scattering by impurities dominates while at higher temperatures the lattice scattering is dominating. This can be seen in the figure 2.6

2.1.5 p-n Junction

Now that we understand how charges behave in the material and how both p-type and n-type doping function, we can consider the effect of combining two materials, one with p-type doping and one with n-type doping, to create a p-n junction.

This type of junction is one of the mechanisms used to facilitate charge separation, which is essential for photovoltaic energy conversion. When two electronically different materials are combined, an electrostatic force arises due to a compositional gradient. In equilibrium, a ‘built-in’ electric field is established at the interface or junction of the two materials. This field plays a crucial role in the charge separation process, driving electrons and holes in opposite directions.

In an equilibrium situation characterized by no external excitation and no net currents, we can consider a junction of two ideal materials, one p-type and one n-type, with a perfect step function instead of a gradient change. When the two materials are placed together at the junction site, charge transfer occurs due to diffusion. Holes diffuse from the p-side into the n-side, and vice versa for the electrons. As the charge carriers leave behind donor and acceptor ions, a positively charged region forms on the n-side of the junction, and a negatively charged region appears on the p-side, immediately adjacent to the junction. This charge gradient produces an electric field ($\mathcal{E}$) that points from the n-side to the p-side, depleting the junction region, referred to as the depletion region (W), of charge carriers by driving them to opposite sides. This assumption considers the region W to be depleted of carriers, with no electric field outside of it, and is known as the depletion approximation.

Figure 2.7 shows schematically the formation of the depletion region W as the neutral regions of p-type and n-type materials come into contact, resulting in the appearance of the electric field $\mathcal{E}$.

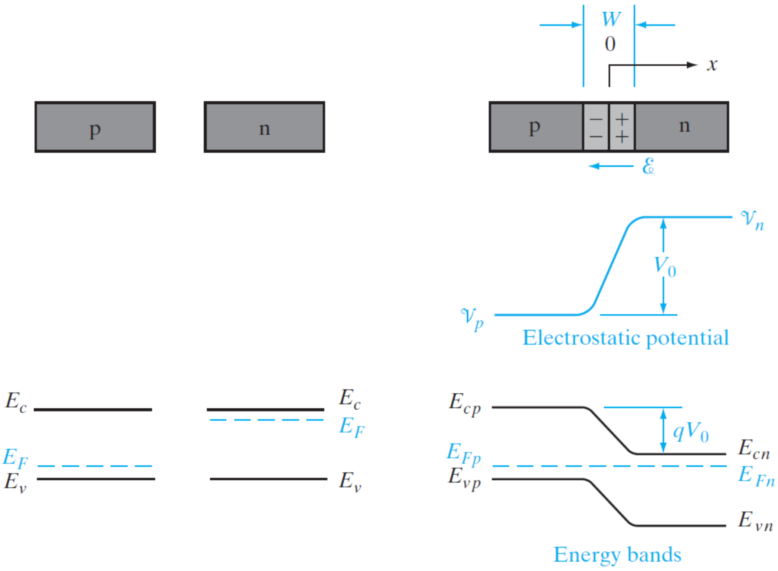

Figure 2.7: Schematic of the isolated p-type and n-type materials (left) and a p-n junction in equilibrium (right) with corresponding energy bands. Adapted from [4].

The electric field appears only within the W region. Since $\mathcal{E} = -\frac{d\mathcal{V}(x)}{dx}$, there is a constant potential $\mathcal{V}_n$ on the n-side, outside of W, and a potential $\mathcal{V}_p$ on the p-side, resulting in a potential difference V_0 between them, known as the contact potential. This is an equilibrium quantity that does not produce any net current. One useful way to relate the concentration of charge carriers to this contact potential is given by the following equation:

$$\frac{p_p}{p_n} = \frac{n_n}{n_p} = e^{\frac{qV_0}{kT}},$$

where p_p and p_n represent the hole concentrations on either side, n_p and n_n are the electron concentrations. Additionally, it is important to note that the Fermi level remains constant across the junction at equilibrium.

Another important factor is the width of the depletion region W, as it is closely related

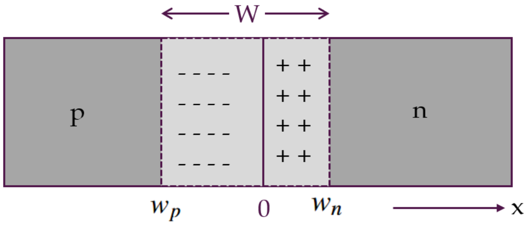

Figure 2.8: Formation of the depletion regions, considering the effect of the difference in doping in the width.

to the working and efficiency of the solar cell. Considering the depletion approximation, it can be shown that this region is described by

$$W = \left[\frac{2\epsilon V_0}{q}\left(\frac{N_a + N_d}{N_a N_d}\right)\right]^{1/2} = \left[\frac{2\epsilon V_0}{q}\left(\frac{1}{N_a} + \frac{1}{N_d}\right)\right]^{1/2}. \tag{2.8}$$

Furthermore, we can determine its extension into both the p and n regions. As will be mentioned later, how far the depletion zone goes into each region is relevant in order to facilitate the transport of charges and avoid recombination processes. The following expressions:

$$\begin{aligned} w_p &= \frac{WN_d}{N_a + N_d} = \frac{W}{1 + \frac{N_a}{N_d}} = \left\{\frac{2\epsilon V_0}{q}\left[\frac{N_d}{N_a\left(N_a + N_d\right)}\right]\right\}^{1/2} \quad \text{and} \\ w_n &= \frac{WN_a}{N_a + N_d} = \frac{W}{1 + \frac{N_d}{N_a}} = \left\{\frac{2\epsilon V_0}{q}\left[\frac{N_a}{N_d\left(N_a + N_d\right)}\right]\right\}^{1/2}, \end{aligned} \tag{2.9}$$

show that the way to increase the extension of W on the p side is by increasing the concentration of donors N_d on the n side and vice versa for the n side with the concentration of acceptors N_a. Figure 2.8 shows an schematic representation of this.

Lastly, it is worth noting that the way to describe the current in a p-n junction in terms of the voltage is given by the diode equation:

$$I(V) = I_0\left(e^{\frac{qV}{kT}} - 1\right), \tag{2.10}$$

where I_0 is a constant dependent on the characteristics of both the p-type and n-type materials, such as diffusion lengths, geometric factors, and the amount of charge carriers. This current is obtained by considering the contributions from the electron and hole currents on their opposing sides and their exponential decrease after leaving the depletion zone.

Equation (2.10) also describes the workings of a p-n junction in the dark. One important feature of a p-n junction is that by applying a forward bias to it, the flow of current can be facilitated from the p-side to the n-side. This means that the forward bias (V_f) lowers the electrostatic potential barrier at the junction as $V = V_0 - V_f$. In the same manner, a reverse bias (V_R) would increase the electrostatic potential barrier at

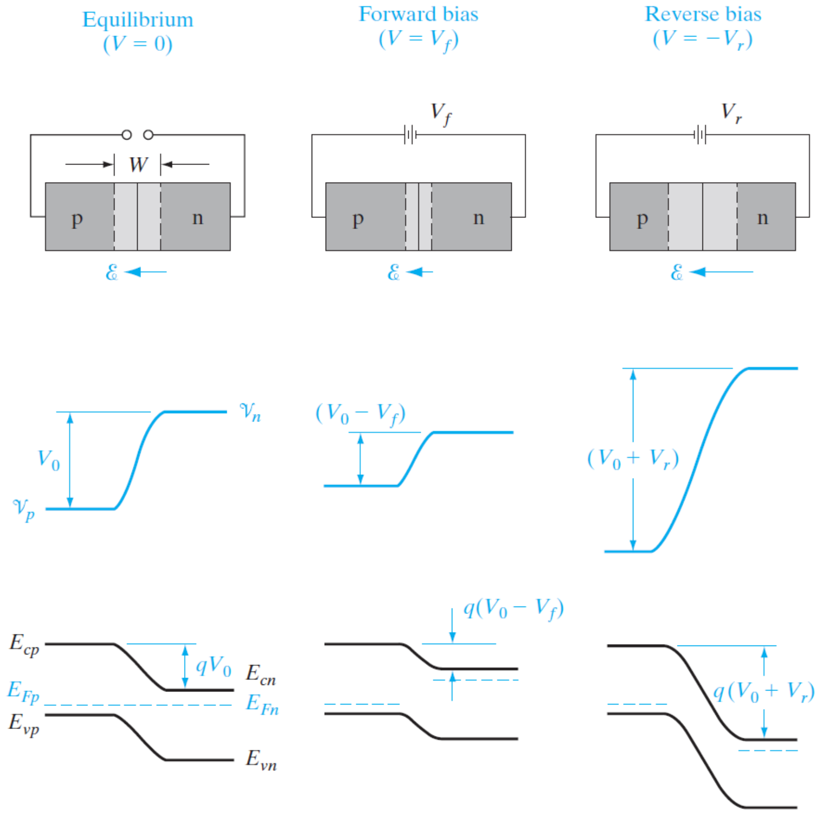

Figure 2.9: Forward and reverse bias representation and effect in the p-n junction. From Streetman and Banerjee [4].

the junction $(V = V_0 + V_R)$. Figure 2.9 illustrates the effect of forward and reverse bias in the p-n junction, while figure 2.10 shows the I-V curve of the p-n junction and the regions corresponding to forward and reverse bias.

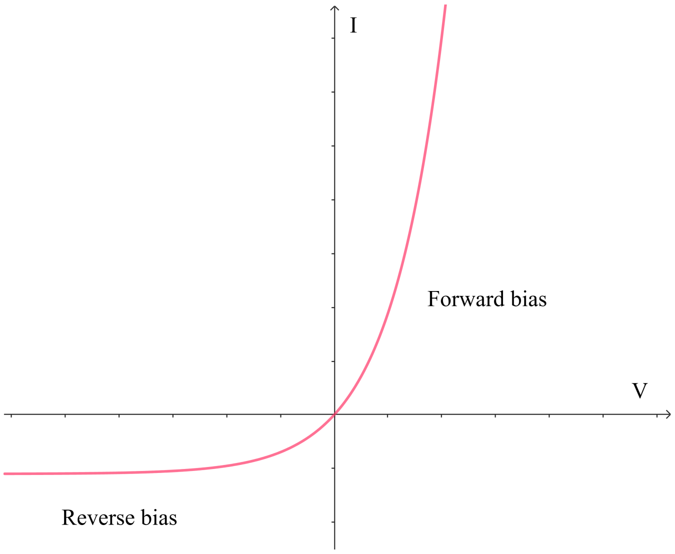

Figure 2.10: I-V curve representation of a p-n junction in the dark, showing forward and reverse bias regions.

2.2 Solar cells

Considering we already know how light can help generate electrons and holes in the conduction and valence bands, respectively, and that these charge carriers can be separated and transported by the creation of a p-n junction, we have all the basis necessary to fully describe the working principle of a solar cell [39].

First, we should consider what happens when we have a p-n junction under illumination.

2.2.1 p-n Junction under illumination

If we consider the junction to be illuminated by photons of $h\nu > E_g$, we can introduce a generation rate g_{op} that is used to determine the number of electrons and holes optically generated per second in the n-region for holes and in the p-region for electrons. The expressions would be AL_pg_{op} for holes and AL_ng_{op}, with L_p and L_n being the diffusion lengths of holes and electrons, respectively, after the depletion region. Additionally, the charge carriers generated inside the depletion region W can be considered as AWg_{op}. All of this together gives the current generated by these carriers as

$$I_{\mathrm{op}} = qAg_{\mathrm{op}}\left(L_p + L_n + W\right), \tag{2.11}$$

which can be placed into the diode equation, so that the current can be expressed as:

$$I = I_{\mathrm{th}}\left(e^{\frac{qV}{kT}} - 1\right) - I_{\mathrm{op}}. \tag{2.12}$$

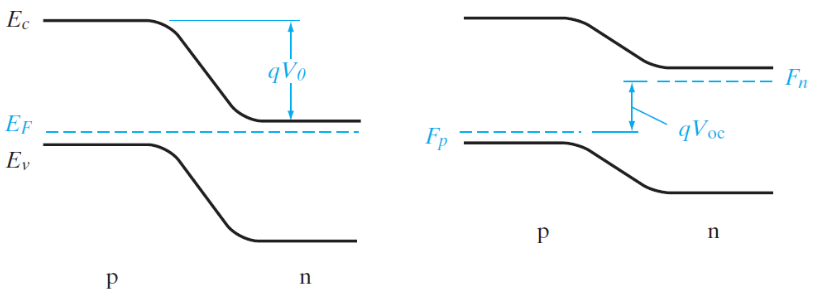

Figure 2.11: Effect of illumination on the p-n junction. From Streetman and Banerjee [4].

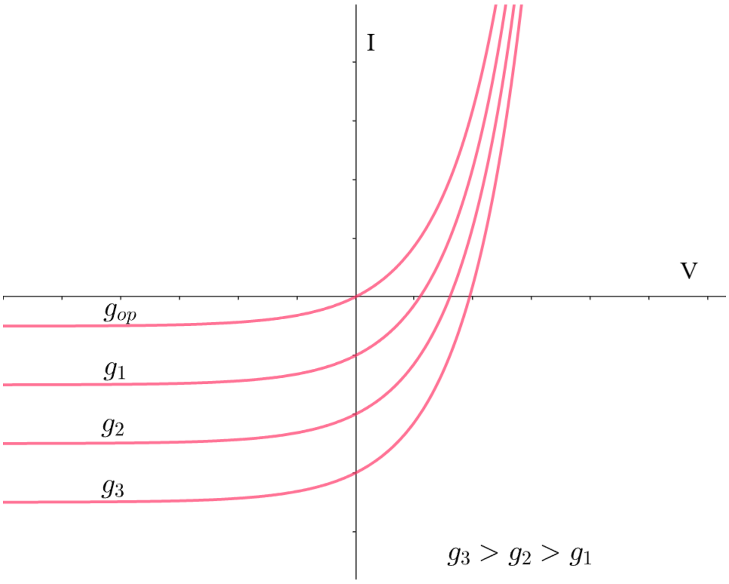

Figure 2.12: I-V curve of a p-n junction under illumination. Based on a graph from Streetman and Banerjee [4].

With I_{th} being the thermally generated current, the I-V curve is lowered on the y-axis as the generation rate increases. We can consider two important values of the I-V curve: the short-circuit current I_{op} and the open-circuit voltage V_{oc}. This voltage, which appears when the junction is under illumination, causes a forward voltage to develop, thereby creating the photovoltaic effect. Figure 2.11 illustrates the appearance of the forward voltage in the p-n junction as it transitions from an equilibrium state and figure 2.12 shows how the I-V curve changes with the generation rate.

2.2.2 Single Junction Solar Cells

From the illuminated junction that we just described, we get some charge carriers that are able to deliver power to an external circuit so that we can convert solar energy into electrical energy. However, the power that can be supplied by one of these cells is less than the band gap voltage E_g/q, which can be quite small. However, a greater number of these cells can be connected in order to increase the power supply, making it a reliable source of electrical power.

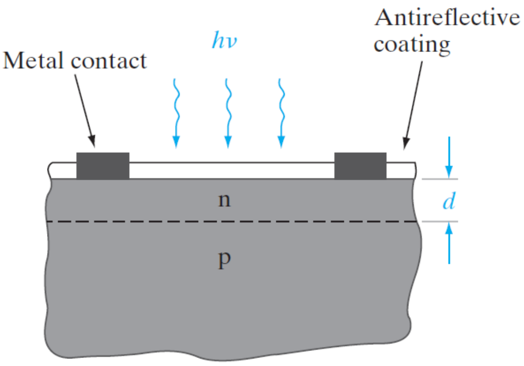

Figure 2.13: Configuration of a solar cell, showing the antireflective coating and contacts. From Streetman and Banerjee [4]

In general, there are some characteristics that we would hope to fulfill in order to optimize the efficiency of a solar cell. In the case of a single junction, we can have either a homojunction, where both the p and n sides of the junction correspond to the same material but are doped to be n-type and p-type correspondingly; or we can have a heterojunction, where two different materials are doped.

Since the efficiency of photovoltaic energy conversion requires optimizing light absorption, charge separation, and charge transport, there are some considerations to take into account. For example, for good optical absorption, we want the reflectivity of the cell to be small; in order to have good charge separation, we want the junction to be close to the surface and the built-in bias to be large; for good charge transport, we want longer carrier lifetimes and diffusion lengths.

To optimize light absorption, we want to have a large junction area close to the surface so that the diffusion length of holes in the n-type material is shorter than the distance to the junction. This ensures that the holes generated near the surface can reach the junction before they recombine. We also want to have a thickness that surpasses the absorption length and a coating on the surface that reduces the reflection of light. Additionally, we want a large contact potential, which implies heavy doping, but heavy doping reduces the lifetimes of the carriers, so a balance must be found.

2.2.3 Shockley Queisser Limit

As a quick note, it is worth mentioning the Shockley-Queisser Limit, although its development won't be shown in this document.

The Shockley-Queisser Limit, presented in 1961 by Shockley and Queisser [40], was the first comprehensive calculation of the theoretical efficiency limit of single-junction solar cells by considering the detailed balance limit. In their calculations, they considered the emission of the sun to be approximate to that of a black body with a temperature of $T_s = 6000\,\mathrm{K}$. Additionally, they considered that only radiative recombination is present, as it is the only spontaneous recombination process and, as such, unavoidable. Thus, recombination sets the limit for the lifetime of carriers.

After a couple more considerations, such as that each photon with energy greater than E_g produces a charge carrier, the efficiency limit for silicon was found to be 26%. However, we know that this value is not the actual limit, as the detailed balance limit model has been modified to be more accurate with what we know today. Considering an AM 1.5G spectrum, Rühle [5] shows conversion efficiencies above 30% for solar cells with band gaps between 0.93 and 1.61 eV.

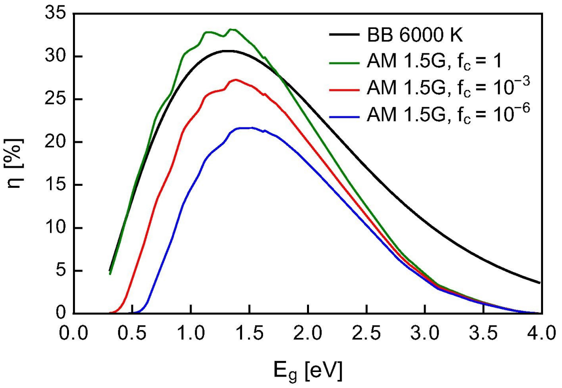

Figure 2.14: Comparison of the Shockley Queisser Limit calculations illuminated by a black body at 6000K (black), with standard solar test conditions considering only radiative recombination (green), and also considering non-radiative recombination 10^3 (red) and 10^6 times stronger than radiative recombination. From Rühle [5].

In order to overcome the limits set by the Shocklet-Queisser Limit, many estrategies have been developed, such as different materials and configurations. Among these, the layering of materials in Tandem configuration is quite important and has shown to increase the efficiency of solar cells [41, 42].

2.2.4 Tandem Solar Cells

One of the biggest problems in using the full solar spectrum is the fact that single-junction solar cells with a determined band gap only absorb and efficiently utilize photons within a certain range of energies. However, if one were to stack materials with various band gaps, photons with higher energies can be absorbed first, while the lower-energy photons can be absorbed and utilized by a second material with a smaller band gap instead of being lost. This way, the power of two junctions can be used and optimized, absorbing a greater range of the solar spectrum.

In order to maximize efficiency, these junctions should be connected independently in a four-terminal connection; however, this is hard to achieve in practice. As such, the most common configuration is the two-terminal connection, where the junctions are connected in series. Figure 2.15 shows these two configurations.

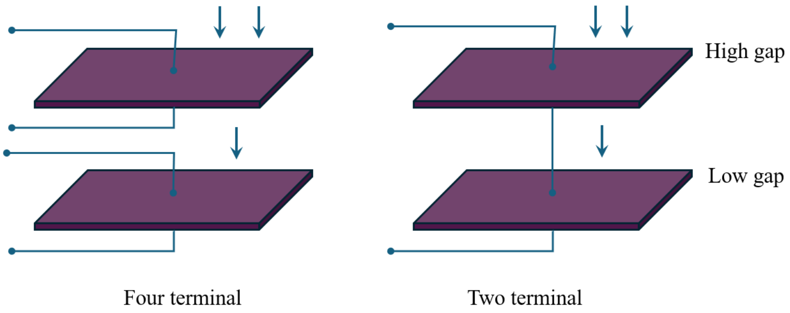

Figure 2.15: Four and two terminal configurations for tandem solar cells, showing that the higher energy photons are prefered for the top cell, while lower energy photons are more utilized in the bottom cell.

Chapter 3

Experimental methods

Various experimental methods were used in this work. The theory behind these methods will be briefly discused in this chapter in order to facilitate the understanding not only of their working, but also of the data that was obtained from the experimental work. As such, this section will discuss the principles of Magnetron Sputtering, Ultraviolet-Visible Spectroscopy (UV-vis), XRD, SEM and EDS. It will also show the specifications of the machines used during this project and the expressions used for the analysis of the results.

3.1 Physical Vapor Deposition

Physical Vapor Deposition (PVD) encompasses vacuum deposition methods in which material transitions from the solid state to vapor and is subsequently 'deposited' as a thin film onto a substrate. PVD has been known for over a century and is pivotal in the evolution of vacuum coating processes [43]. This process is widely used across various industries, accommodating substrates such as metal, ceramics, glass, and polymers. The vapor or gas production can occur through evaporation, sputtering, or other non-chemical methods.

Generally, the process involves transferring kinetic energy to atoms in solid or liquid form until their binding energy is surpassed [6]. The main methods include:

- Evaporation: Heating a material until its atoms vaporize. Heating sources range from resistive heated wires to complex ovens or electron-beam heaters.
- Sputtering: Physical impacts transfer kinetic energy and momentum to the atoms in a target until they gain sufficient energy and momentum to break free from the surface.

Since sputtering is the most pertinent method for this project, the focus will be on it.

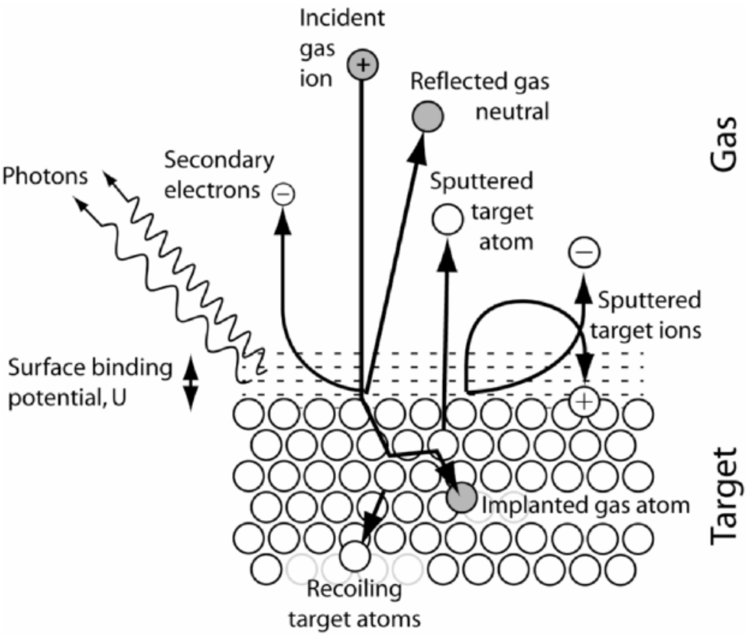

Figure 3.1: Schematic of the sputtering process. From Rockett [6].

3.2 Sputtering

In solids, electronic bonding between atoms results in a binding potential at the surface. To sputter atoms from the target, energy exceeding the binding potential must be imparted to the surface atoms. Additionally, the atoms' momentum must be directed outward from the target's surface for successful escape. This process is schematically illustrated in Figure 3.1.

When bombarding the target surface with accelerated atoms, not only may atoms of the material be sputtered, but some particles may be emitted as charged ions, useful for the Secondary-Ion Mass Spectroscopy (SIMS) technique. If the target atoms are significantly heavier than the bombarding atoms, some ions may be reflected by the target. As shown in Figure 3.1, the ion bombardment of the target surface can also result in secondary electron emission, photon emission, reflected gas neutrals, recoiling target atoms, implanted gas atoms, and heating of the target due to inelastic processes [6].

3.2.1 Sputtering Systems

Sputtering systems are categorized based on how energy is supplied to the gas to form ions that bombard the target. These systems are divided into direct current (DC) and radio frequency (RF) types. The system includes two contacts to the gas: the target, which functions as a cathode, and an anode, which is considered the rest of the grounded system. Some systems may include an additional electrode, which can be either an anode or a cathode, resulting in 'triode' sputtering [6]. A schematic diagram of this system is shown in Figure 3.2.

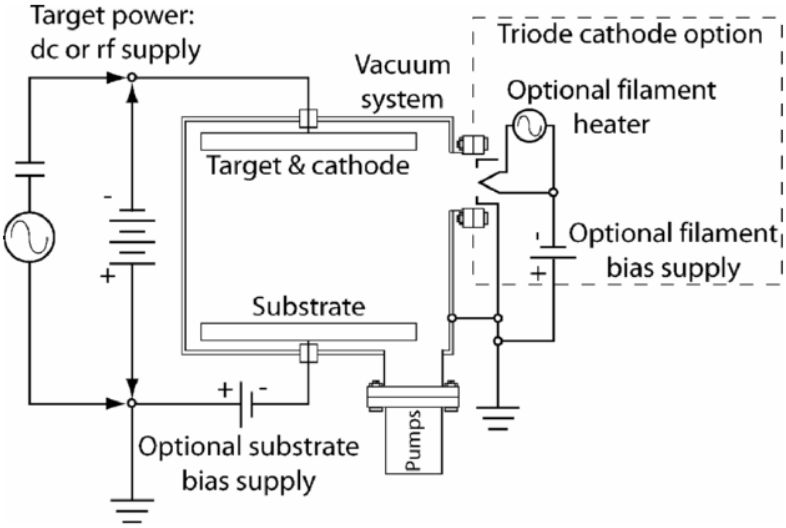

Figure 3.2: Schematic diagram for sputtering systems with DC or RF power supply. From Rockett [6].

The choice between DC and RF current depends on the sputtering machine used and the target material. This choice affects the sputtering rate, as DC typically results in a higher rate than RF [44, 45]. This could be considered as an intrinsic characteristic of the RF power supply, Nyaiesh and Holland [44] propose this to be related to a different discharge power distribution between the DC and RF modes. DC current is the cheapest and most basic of the systems, however it requires for the target material to be very conductive, or it could indulge in target poisoning by the accumulation of charge inside it, stopping altogether the sputtering process. Due to this, RF sputtering can be used to combat these issues, in that case, the current is alternated with radio frequency so that there's no charge build up inside the target. Another option is to use High-Power Impulse Magnetron Sputtering (HIPIMS), which uses a very high voltage in short times to make a high density plasma around the target [46].

To increase the sputtering rate, which is related to the ion flux hitting the target, one can increase the ion density in the gas. The most common method to achieve this is by using magnets to redirect electrons leaving the target, improving their efficiency at ionizing atoms along their path. These magnets are positioned behind the targets, as shown in Figure 3.3, forming magnetic field loops. This configuration creates a zone close to the targets where the ion gas density is significantly higher than the rest of the chamber, ensuring that sputtering occurs predominantly on the target, thus increasing overall efficiency. When this configuration is used, it's said that one is using Magnetron sputtering.

Additionally, it's worth mentioning that the sputtering usually happens while in an atmosphere of an inert gas, normally Argon, but in some cases it is wanted to have reactive sputtering. Reactive sputtering happens when there's a reactive gas also inside

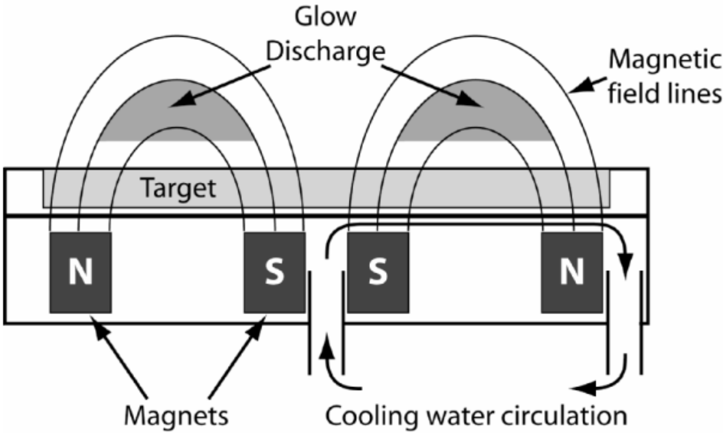

Figure 3.3: Schematic diagram of the magnetic field around the target material in a magnetron sputtering.

the chamber with the inert gas. This gas, that could be oxygen, nitrogen, etc., for example, interacts with the sputtered atoms so that a compound film is grown on the substrate, such as oxides or nitrites [47].

In the case of this work, the deposition happened in two different magnetron sputters, that can be introduced by their nicknames: NanoPVD and Moorfield (figure 3.4). The first one, NanoPVD had both an RF and a DC source that worked simultaneously in order to sputter Zn and Cu atoms. The second magnetron sputter, Moorfield, had two RF sources working simultaneously and had different preassure settings. The deposition was done in an argon and oxygen atmosphere, by reactive sputtering, in order to deposit $Cu_xZn_{1-x}O$ in various concentrations of copper and zinc (x). This will be further shown in Chapter 4.

Figure 3.4: NanoPVD magnetron sputter (left) and Moorfield magnetron sputter (right)

3.3 UV-vis

Ultraviolet-Visible Spectroscopy (UV-vis), as the name implies, uses radiation that covers the Ultraviolet and Visible parts of the electromagnetic spectrum, sometimes up to the near-infrared, covering ranges from 200 to 2500 nm, in order to determine the optical properties of various materials. For semiconductors, the optical properties, such as reflection, transmission, and absorption, are linked to their characteristic band structures, and they can give information corresponding to the energy states near the valence and conduction band, and as such, to the forbidden energy levels of the band gap E_g [48, 49].

In general, there are various ways of determining the band gap of a semiconductor, such as electrical conductivity, Hall effect, or photoconductivity. However, these methods are either temperature-dependent or surface-sensitive. On the other hand, optical spectroscopy methods present some advantages by being non-destructive, contactless in some cases, and require minimal or no sample preparation [49].

In this work, the spectrophotometer Shimadzu SolidSpec-3700 DUV, figure 3.5, was used to obtain transmittance and reflectance values for the samples under study. These results were used to determine the absorption coefficient and, subsequently, to estimate the band gap values using the Tauc plot. The spectra were taken covering a wavelength range from 290 nm to 2500 nm in 1 nm steps.

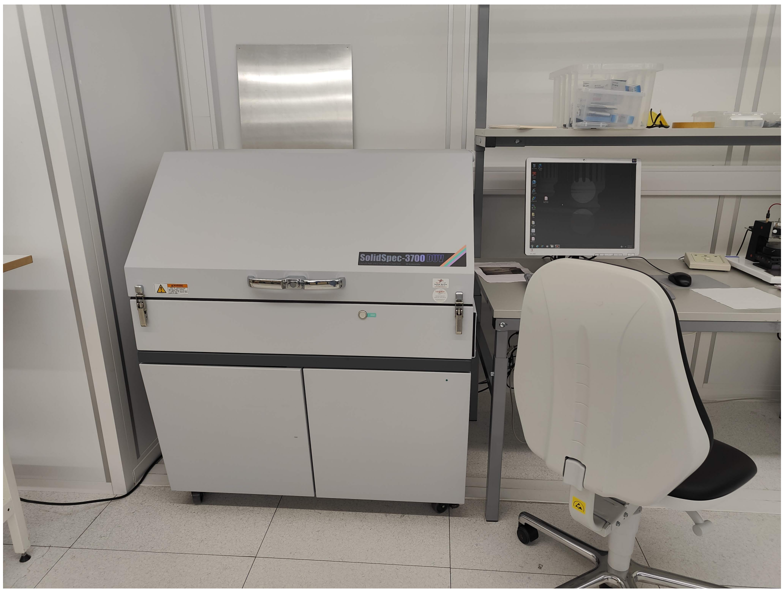

Figure 3.5: Shimadzu SolidSpec-3700 DUV with an integrating sphere found at MiNaLab. Suitable for transmission, reflection, and scattering measurements of thin films.

Absorption coefficient determination

To determine the band gap values using optical methods, it is essential to obtain the absorption coefficient α. To achieve this, we must consider the interaction of light with the sample upon incidence.

When an incident beam reaches a material, the light undergoes three processes: it is partially reflected by the material, some is transmitted through the material, and some is absorbed by the material. This phenomenon can be expressed as follows:

$$T\% + R\% + A\% = 100\%, \tag{3.1}$$

where T is the transmittance, R is the reflectance, and A is the absorbance. Then, considering the Beer-Lambert law

$$\begin{aligned} I &= I_0\, e^{-\alpha d} \\ T &= \frac{I}{I_0} = e^{-\alpha d}, \end{aligned} \tag{3.2}$$

with I is the intensity of the transmitted light, I_0 is the intensity of the incident light, and d is the thickness of the sample. This relationship provides an expression that connects the transmittance of the sample to the absorption coefficient. If we also take into account the reflectance, one way to relate these quantities is through the following expression [50, 51]:

$$T + R = \ e^{-\alpha d}, \tag{3.3}$$

we can derive an expression for the absorption coefficient from the previous equation:

$$\alpha = (\ln (T + R))/d, \tag{3.4}$$

the expression 3.4, in conjunction with the Tauc Plot, allowed us to determine the band gap values.

Tauc plot obtention

To derive an expression for the Tauc plot, we must consider the energy of the incident photons, given by $E = h\nu$, where h is the Planck constant and ν is the photon frequency. This energy is a crucial factor in determining the band gap. Ideally, in materials with a direct band gap, where there is no need for changes in crystal momentum, we expect the absorption coefficient (α) to behave as

$$\begin{aligned} &\alpha(E < E_{gap}) = 0 \\ &\alpha(E \geq E_{gap}) \propto (E - E_{gap})^{1/2}. \end{aligned} \tag{3.5}$$

However, if the material has an indirect band gap, the transition involves phonons due to changes in the momentum, then we can expect it to behave differently for photons of energy values greater than the band gap

$$\alpha(E \geq E_{gap}) \propto (E \pm \hbar\Omega - E_{gap})^2, \tag{3.6}$$

where $\pm\hbar\Omega$ is the energy of a phonon being emitted or absorbed [49]. In most situations, this value can be neglected. Considering this, the Tauc plot [52, 53] follows the assumption that α can be expressed as

$$(\alpha h\nu)^{1/\gamma} = B(h\nu - E_g), \tag{3.7}$$

with a constant B and a factor γ that establishes the electronic transition. γ is equal to 1/2 for direct transitions and 2 for indirect transitions. Therefore, to determine the energy of the forbidden band of a material with an indirect band gap, we use the following expression for the Tauc plot:

$$(\alpha h\nu)^{1/2} = B(h\nu - E_g), \tag{3.8}$$

while, in the case of a material with a direct band gap, the expression is

$$(\alpha h\nu)^2 = B(h\nu - E_g). \tag{3.9}$$

In both cases, the method to determine the band gap involves fitting the linear portion of the curve and finding E_g as the point where this line intersects the x-axis.

It is important to note that in some materials, a distinction exists between the energy required to create an electron-hole pair, referred to as an exciton, and the energy needed to separate them. This leads to the concept of an ‘optical band gap’, associated with the energy of a photon being absorbed, as opposed to the ‘electronic band gap’, which represents the actual energy needed to separate the electron-hole pair. However, in most inorganic semiconductors, the binding energy of the electron-hole pair is sufficiently small that this difference can often be neglected [54, 55].

3.4 X-Ray Diffraction

X-Ray Diffraction (XRD) is very powerfull techinique that is widely used in order to determine and study the molecular and atomic structure of crystalline materials.

In general, crystals are composed of atoms that are organized in a regular array. On the other hand, X-rays are electromagnetic waves. When these waves collide with the atoms, they are elastically scattered, generating waves. These waves interfere with each

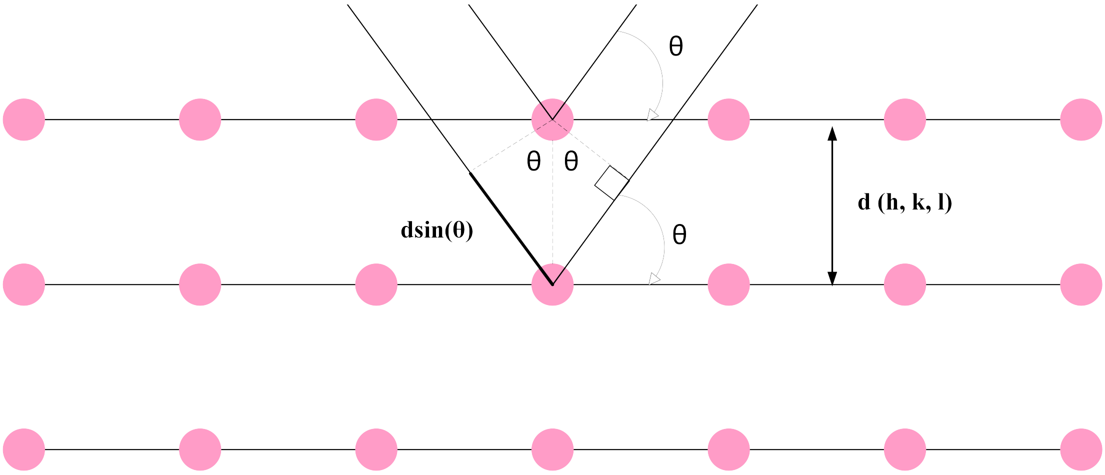

Figure 3.6: Schematic representation of Bragg's Law.

other and can generate either constructive, where they add on, or destructive, where they cancel each other, interference. This process is dependent on the angle of incidence of the x-rays colliding with the atoms, as is shown by the Bragg model of diffraction [56].

In the Bragg model of diffraction, we have an incoming x-ray with a wavelength λ that collides with a crystal lattice with a separation between crystal planes d at an angle θ. This can be seen in the figure 3.6. There are specific angles at which the waves produce constructive interference; in those cases, Bragg's law applies:

$$n\lambda = 2d\sin\theta, \ \ n = \pm 1, 2, 3... \tag{3.10}$$

The change in the angle can be plotted with the intensity of the signal, giving a diffraction pattern where the intensity spikes for the angles at which constructive interference occurs [56].

For the X-ray measurement, we have used a Rigaku SmatLab 3kW high-resolution X-Ray Diffractometer, figure 3.7. This diffractometer is equipped with a HyPix-3000 (horizontal) detector and operates with an X-Ray generator at 40 kV and 50 mA. The data were obtained using grazing incidence X-ray diffraction Grazing Incidence X-ray Diffraction (GIXRD).

3.4.1 Grazing Incidence X-Ray Diffraction

GIXRD is a technique in which the x-ray beam grazes the sample, entering it at small angles of incidence. This configuration allows the X-rays to only enter the most superficial layers, making it useful for the analysis of thin films while ignoring or minimizing the interference of the substrate or bulk material. This way, GIXRD increases the structure information that we can get from polycristalline thin films [57].

GIXRD follows the same principles as normal XRD, but considers the case in which the angle between the incident beam and the surface of the same is very small and it

Figure 3.7: Rigaku SmartLab 3kW high-resolution X-ray Diffractometer found at UiO MiNaLab

is kept constant through the measurement. Then, the detector is moved along the 2θ circle, where 2θ is the scattering angle [57].

In this project, the GIXRD experiment was conducted in a parallel beam configuration without a monochromator, using a continuous scan mode. The scan range extended from 20 - 90^o in increments of 0.05° and a scanning speed of 2.0 °/min. This setting was constant for all samples, and it was used to determine the structure and phases present in the samples, as well as the changes due to heat treatments.

3.5 Scanning Electron Microscopy

Several techniques within optical microscopy enhance both the scale and level of detail observable under a microscope. Among them, the Scanning Electron Microscopy (SEM) stands out for its ability to produce high-resolution images and achieve significant magnification, reaching the atomic scale. The SEM operates based on the interaction between a focused electron beam (e-beam) and the surface atoms of a sample. The resulting signals are captured by detectors and processed to generate high-definition images [58, 59].

The way the SEM works goes as follows: an e-beam, typically generated by a tungsten or LaB_6 cathode, scans the surface of a sample, leading to interactions between the incident electrons and the electrons of the sample. These interactions give rise to a couple processes that are important, the first one is when the incident electrons, also called primary electrons, are scattered by the atoms of the sample at a wide angle (over 90^o). These electrons are the ones that are collected by a detector and form an image of the sample, they are called backscattered electrons [60, 61].

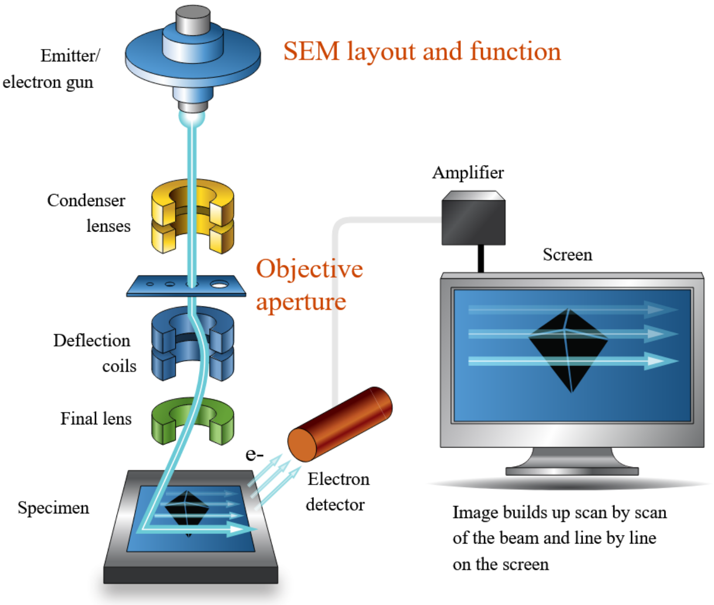

Figure 3.8: Schematic representation of the SEM layout and functioning [61].

The second process happens when these primary electrons give their energy to electrons bound to the atoms of the sample, then these electrons can be ejected from their orbitals and can move through the sample, and if they are close enough to the surface, they can exit the sample. These electrons are called secondary electrons and can also be collected by a detector and generate an image of the surface of the sample [60, 61].

While both backscattered and secondary electrons can form an image of the surface of the sample, since heavy elements tend to scatter primary electrons more strongly, then an image generated by the backscattered electrons can show changes in the chemical composition in the form of a contrast. Meanwhile, secondary electrons that are generated close to the surface of the sample, when collected by the detector, give a signal that can be used for topographical determination of the sample. Secondary electrons that are generated further down the sample usually undergo a series of collisions that make them lose their energy before escaping the sample [60, 61].

In general, the e-beam would generate not only secondary electrons and backscattered electrons, but also X-rays and Auger electrons. Of these, X-rays are particularly interesting as they are used in Energy Dispersive Spectroscopy (EDS). A schematic representation of a scanning electron microscope is shown in Figure 3.8.

Scanning electron microscopy is widely used for analyzing surface morphology, texture, and composition across a range of materials, including metals, ceramics, polymers, and even organic substances, provided they are conductive. This technique is particularly advantageous due to its non-destructive nature and broad applicability, as the primary requirement for analysis is that the sample exhibits electrical conductivity, which can also be obtained by coating the sample with a thin metal layer[61].

Compared to conventional optical microscopes, SEM offers significantly higher magnification, exceeding 300,000x, along with an extended depth of field, reaching up to 4 mm, and superior resolution, down to 0.4 nm. These specifications greatly surpass those of optical microscopy, which typically achieves magnifications of up to 1,000x, a depth of field of approximately 15 μm, and a resolution limit of 0.2 μm [58, 59].

3.5.1 Energy Dispersive X-Ray Spectrometry

As mentioned before, the incident electrons can also generate x-rays, which can be used in Energy Dispersive Spectroscopy (EDS). If we consider the Bohr atomic model, then, when a secondary electron is emitted from a core shell of an atom, then an electron from a higher energy shell can fall to that newly empty level to minimize its energy. When this happens, the energy, which is characteristic for this transition, is emitted in the form of an x-ray which can be detected and measured [62, 63].

This way, the x-rays emitted by the sample act in the form of a fingerprint of the atom, giving specific information about their chemical composition. However, this technique is quite low in sensitivity compared to other chemical analysis techniques [63].

One of the main advantages of EDS is that it is a fast and non-destructive technique with minimum requirements to be used.

In this work, to determine the composition of the samples, a scanning electron microscope was used to perform EDS. Figure 3.9 shows the microscope used, a JEOL IT-300 with a LaB_6 electron gun. The acceleration voltage was set at 3 keV to make the Zn and Cu peaks more intense and relevant compared to the Si peaks. Then later, the program Pathfinder X-ray microanalysis software was used to identify the peaks and quantify the composition of the samples. The values obtained were normalized to the sum of Zn and Cu in order to determine the x in the system $Cu_xZn_{1-x}O$.

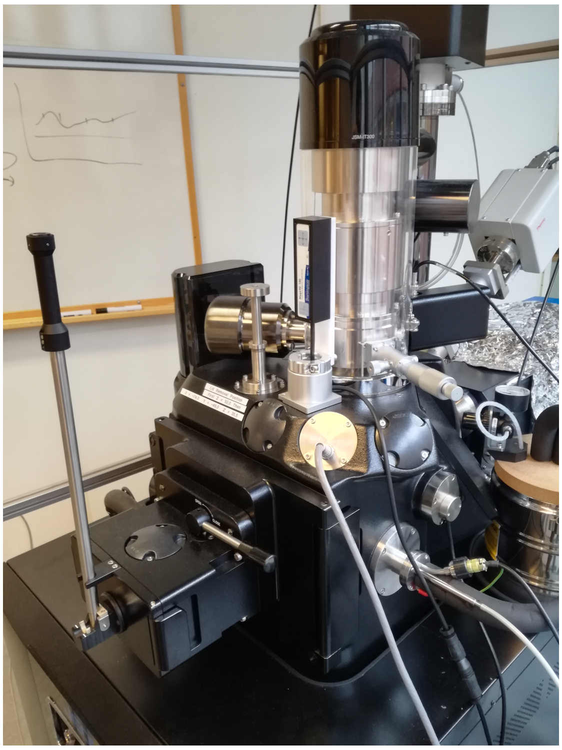

Figure 3.9: Scanning Electron Microscopy (SEM) instrument is found at MiNaLab. Suitable for high-resolution imaging, semi-quantitative X-ray microanalysis, as well as cathodoluminescence imaging and spectral analyses.

Chapter 4

Analysis and Results

4.1 Samples details

We have already discussed the general principles of thin film deposition in Section 3.1. In this section, we will outline the specific steps followed to obtain the samples used in this project and how they will be distinguished during this chapter.

In general, the samples follow the composition $Cu_xZn_{1-x}O$. To achieve this composition, targets of 99.99% Cu and 99.99% Zn were utilized. The power applied to each target was varied to generate the desired variation in composition between Zn and Cu. The thin films were deposited using reactive sputter deposition in an atmosphere of both oxygen and argon on fused silica substrates, which are 0.5 mm thick and 20 by 20 mm in size.

To begin, we can divide the deposition process into two parts based on the machines used for sample preparation. First, we introduce the two machines by their names: NanoPVD and Moorfield. Both are magnetron sputters belonging to the MinaLab at UiO and can be seen in the figure 3.4. The reason for this differentiation is that certain changes were dependent on the characteristics of the machines, which will be discussed shortly.

Table 4.1: Deposition parameters summarization for all batches of samples, showing partial pressure of oxygen and argon atmospheres (P_{O2} and P_{Ar}, respectively) as well as the total pressure during deposition (P_T)

Batch #	Number of Samples	Temperature °C	$Ar:O_2$ sccm:sccm	P_{O2} mTorr	P_{Ar} mTorr	P_T mTorr
1	8	200	20:2.5	3.00	15.30	18.30
2	6	200	20:2.5	0.20	5.40	5.40
3	5	200	10:10	1.00	5.60	6.40
4	7	400	10:10	1.00	5.60	6.40
5	7	600	10:10	1.00	5.60	6.40

Furthermore, we will classify the samples into batches, where each batch will exhibit variations in composition (x) while keeping parameters such as temperature, deposition time, and atmosphere mostly consistent. Table 4.1 summarized the values that remained constant for each batch of samples, such as the total and partial pressures (P_T, P_{O2} , and P_{Ar}), and temperature.

Table 4.2: Samples per batch obtained by varying the power applied to both copper and zinc targets (P_{Cu} and P_{Zn}, respectively), and the changes in thickness and composition by atomic percentage (x). The values of magnetron power marked with an asterisk were obtained from a DC power source.

Batch #	Sample name	P_{Zn} W	P_{Cu} W	Thickness (±5 nm)	x (%atom.)
1	CZ01a	54*	0	110	0.00
	CZ01b	49*	78	140	0.19
	CZ01c	23*	78	60	0.50
	CZ01d	0	80	30	1.00
	CZ01e	0	65*	335	1.00
	CZ01f	78	64*	410	0.82
	CZ01g	78	28*	70	0.62
	CZ01h	80	0	34	0.00
2	CZ02a	0	150	420	1.00
	CZ02b	50	100	380	0.75
	CZ02c	75	75	390	0.49
	CZ02d	100	50	400	0.19
	CZ02e	125	25	400	0.05
	CZ02f	150	0	300	0.00
3	CZ03a	0	100	70	1.00
	CZ03b	25	75	70	0.84
	CZ03c	50	50	70	0.42
	CZ03d	75	25	60	0.10
	CZ03e	100	0	60	0.00
4	CZ04a	0	100	35	1.00
	CZ04b	25	75	50	0.85
	CZ04c	38	62	55	0.71
	CZ04d	50	50	30	0.47
	CZ04e	62	38	30	0.34
	CZ04f	75	25	45	0.10
	CZ04g	100	0	45	0.00
5	CZ05a	0	100	60	1.00
	CZ05b	25	75	75	0.87
	CZ05c	38	62	60	0.76
	CZ05d	50	50	70	0.54
	CZ05e	62	38	40	0.36
	CZ05f	75	25	60	0.12
	CZ05g	100	0	80	0.00

Additionally, table 4.2 shows the parameters that vary per sample, such as the power applied to the zinc and copper targets (P_{Cu} and P_{Zn}, respectively). It also shows some of the results from the initial characterization process, with the thickness of the samples (δ) and the composition by atomic percentage (x).

First batch of samples:

The first set of samples was obtained using NanoPVD. To vary the composition of the samples, the percentage of power applied to each target was adjusted. However, this machine had both a DC power source and an RF power source that could be used simultaneously. To obtain equivalent values for x, the type of power source for each target was switched after half of the first set of samples had been produced. These samples were fabricated using reactive sputter deposition in an Ar:O_2 atmosphere with a ratio of 20 : 2.5 SCCM, a substrate temperature of 200 °C, and an intended deposition time of 60 minutes for each sample.

Power control in the NanoPVD machine was managed as a percentage of the total available power, which corresponded to 75-80 W for the RF source and 20-65 W for the DC source. Generally, the RF source was maintained at 80 W, equivalent to 50% of the total power of the power supply unit (PSU), while the DC source was varied between 0%, 5%, and 10% of the total PSU. This resulted in power levels of 0 W, 23 W, and 49 W for the Zn target, and 0 W, 28 W, and 64 W for the Cu target.

During this process, we observed that the plasma generated on the DC-powered target tended to be unstable, frequently shutting down multiple times throughout the deposition period. Due to this instability, we switched to the Moorfield magnetron sputter for the second and subsequent batches of samples. This change necessitated adjustments to the deposition parameters.

After these samples were characterized by EDS, XRD, and UV-vis, they were annealed and characterized once again. A tube furnace, figure 4.1, was used to reach a temperature of 400 °C. The samples were introduced once the desired temperature was achieved and left in the oven for one hour. This process was initially intended to be applied to different batches of samples at various temperatures. However, since the changes observed in the results were not as expected, the focus shifted to the temperature during deposition for batches three, four and five.

Second Batch of Samples:

For the second batch of samples, we switched to a different magnetron sputter, which had two RF power sources. This allowed us to apply equivalent power to both the Zn and Cu targets without any issues. We maintained the same atmospheric conditions, using reactive sputter deposition in an Ar:O_2 with a ratio of 20 : 2.5 SCCM and a substrate temperature of 200 °C. We increased the RF power so that a total of 150 W was applied between both targets, reducing the deposition time to 30 minutes.

Figure 4.1: Tube Furnace at MiNaLab

This process was significantly more stable; however, we observed that the atmospheric conditions did not have the optimal proportion of O_2 and Cu (as will be shown in more detail in the section 4). This resulted in the formation of Cu_2O phases in the thin film. Consequently, we adjusted these conditions for the next batch of samples and changed the power range.

Third Batch of Samples:

For this batch most of the settings and parameter were kept the same as for the second one, only changing the atmosphere of Ar:O_2 from a ratio of $20 : 2.5$ SCCM to $10 : 10$ SCCM and a total power range of 100 W, instead of 150 W, between both targets, varying in steps of 25 W for a total of 5 samples.

As this batch of samples gave good results during the characterization, it was decided to proceed with these parameters for following batches, varying only the deposition temperature.

Fourth Batch of Samples:

This batch had the same parameters as the third one, with only a change in the deposition temperature from 200 °C to 400 °C . This means: 100W in total power between both targets, 30 minutes depositions, and atmosphere of Ar:O_2 with a ratio of $10 : 10$ SCCM. However, two extra samples at intermediate powers were added, reducing the steps in power close to the 50–50 W sample.

Fifth Batch of Samples:

This last batch had the same parameters as the previous one, but the deposition temperature was set at 600 °C , with a total of seven samples with varying composition as was previously explained.

4.2 Composition and thickness determination.

For each sample, EDS was used in order to obtain the composition (x) of the samples. Figure 4.2 shows an example of the results obtained from the EDS measurements, where we can see the changes in the peaks corresponding to Zn and Cu as the x changes.

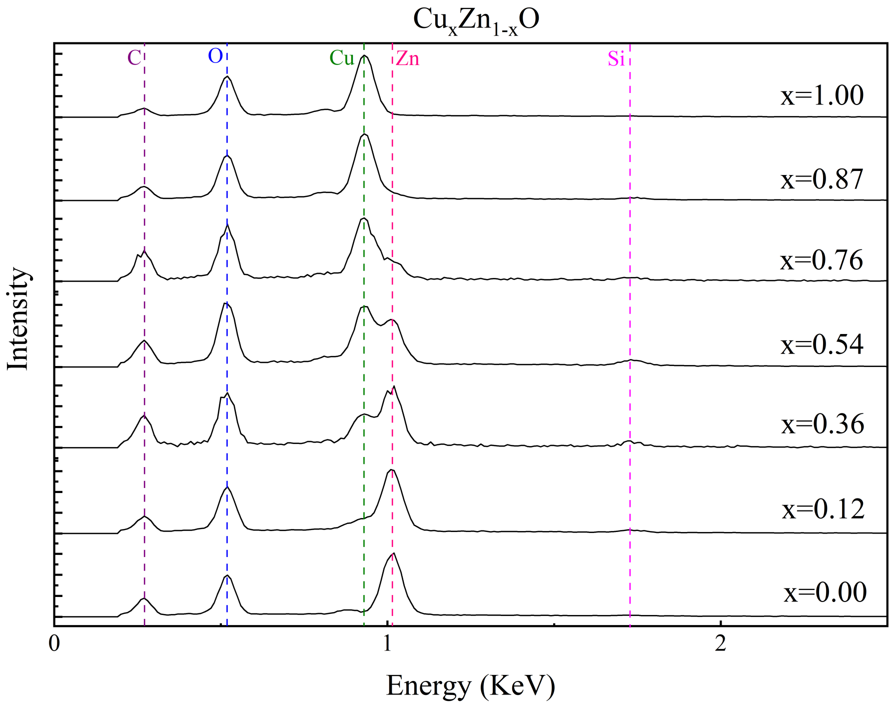

Figure 4.2: EDS spectrum obtained from the fifth batch of samples.

Additionally, a profilometer was used in order to determine the thickness of each sample. Figure 4.3 shows an example of of the profilometer scan data. By averaging the height in the higlighted zones and susbtracting the resulting values we determined the thickness of each sample.

Tables 4.3, 4.5, 4.6, 4.8 and 4.10 shows the composition determination for each batch of samples. The tables present the proportions of copper, oxygen and zinc of each sample, then these values are normalized to only show proportion between copper and zinc which was used to determine the x in $Cu_xZn_{x-1}O$. Additionally, the thickness of the samples were determined, as well as the growth ratio, considering the deposition time. These values can be seen in the tables 4.4, 4.7, 4.9 and 4.11.

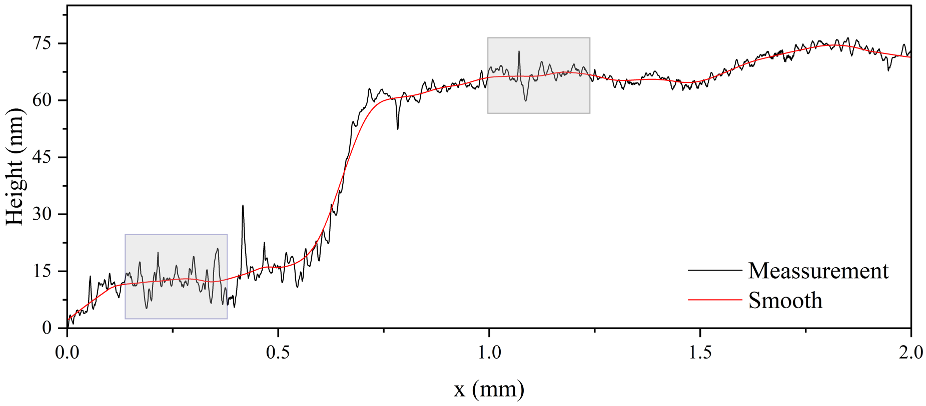

Figure 4.3: Profilometer scan data

Table 4.3: Determination of the composition of the first batch of samples, considering the form $Cu_xZn_{x-1}O$. First there is the percentage of copper, zinc and oxygen, then this was normalized to get the proportions between zinc and copper, which were used to determine the *x*. The first four samples, marked with *, were deposited with Zn in the DC power source and the last four with the Cu target in the Dc power source.

Cu ±1.2 %	Zn ±1.1 %	O ±0.7 %	Cu (norm.) ±2.0 %	Zn (norm.) ±2.0 %	$Cu_xZn_{x-1}O$ x
0.0	47.3	52.7	0.0	100.0	0.00*
9.4	40.7	49.9	18.8	81.2	0.19*
25.1	25.2	49.7	49.9	50.1	0.50*
53.8	0.0	46.2	100.0	0.0	1.00*
68.7	0.0	31.3	100.0	0.0	1.00
45.2	10.2	44.5	81.5	18.5	0.82
33.1	19.8	47.1	62.5	37.5	0.62
0.0	51.5	48.5	0.0	100.0	0.00

Table 4.4: Thickness and growth ratio of the first batch of samples. The first four samples were deposited with Zn in the DC power source and the last four with the Cu target in the DC power source.

Composition x	Thickness ±5 nm	Growth ratio nm/min
0.00	110	1.8
0.19	140	2.3
0.50	60	1.0
1.00	30	0.5
1.00	335	5.6
0.82	410	7.9
0.62	70	2.6
0.00	35	0.6

Table 4.5: Determination of the composition of the second batch of samples, considering the form $Cu_xZn_{x-1}O$. First there is the percentage of copper, zinc and oxygen, then this was normalized to get the proportions between zinc and copper, which were used to determine the x.

Cu ±1.8 %	Zn ±1.6 %	O ±0.8 %	Cu (norm.) ±2.0 %	Zn (norm.) ±2.0 %	$Cu_xZn_{x-1}O$ x
73.3	0.0	26.7	100.0	0.0	1.00
47.2	15.7	37.1	75.1	24.9	0.75
30.9	31.7	37.5	49.4	50.6	0.49
11.1	48.4	40.5	18.7	81.3	0.19
3.1	58.5	38.4	5.1	94.9	0.05
0.0	51.5	48.5	0.0	100.0	0.00

Table 4.6: Determination of the composition of the third batch of samples, considering the form $Cu_xZn_{x-1}O$. First there is the percentage of copper, zinc and oxygen, then this was normalized to get the proportions between zinc and copper, which were used to determine the x.

Cu ±1.8 %	Zn ±0.7 %	O ±0.9 %	Cu (norm.) ±1.2 %	Zn (norm.) ±1.2 %	$Cu_xZn_{x-1}O$ x
55.9	0.0	44.1	100.0	0.0	1.00
46.8	8.8	44.4	84.2	15.8	0.84
22.9	31.0	46.1	42.5	57.5	0.42
5.0	47.2	47.8	9.5	90.5	0.10
0.0	51.2	48.8	0.0	100.0	0.00

Table 4.7: Thickness and growth ratio of the third batch of samples.

Composition x	Thickness ±5 nm	Growth ratio nm/min
1.00	70	2.3
0.84	70	2.3
0.42	70	2.3
0.10	60	2.0
0.00	60	2.0

Table 4.8: Determination of the composition of the fourth batch of samples, considering the form $Cu_xZn_{x-1}O$. First there is the percentage of copper, zinc and oxygen, then this was normalized to get the proportions between zinc and copper, which were used to determine the x.

Cu ±2.8 %	Zn ±2.5 %	O ±1.2 %	Cu (norm.) ±3.8 %	Zn (norm.) ±3.8 %	$Cu_xZn_{x-1}O$ x
56.5	0.0	43.5	100.0	0.0	1.00
48.1	8.5	43.4	85.0	15.0	0.85
33.9	13.8	38.9	71.0	29.0	0.71
25.8	29.4	44.7	46.7	53.3	0.47
13.2	25.7	40.6	34.0	66.0	0.34
5.1	46.9	48.0	9.8	90.2	0.10
0.0	51.7	48.3	0.0	100.0	0.00

Table 4.9: Thickness and growth ratio of the fourth batch of samples.

Composition x	Thickness ±5 nm	Growth ratio nm/min
1.00	35	1.2
0.85	50	1.7
0.47	30	1.0
0.10	45	1.5
0.00	45	1.5
0.75	55	1.8
0.35	30	1.0

Table 4.10: Determination of the composition of the fifth batch of samples, considering the form $Cu_xZn_{x-1}O$. First there is the percentage of copper, zinc and oxygen, then this was normalized to get the proportions between zinc and copper, which were used to determine the x.

Cu ±2.8 %	Zn ±2.6 %	O ±3.3 %	Cu (norm.) ±4.0 %	Zn (norm.) ±4.0 %	$Cu_xZn_{x-1}O$ x
56.6	0.0	43.4	100.0	0.0	1.00
49.7	7.6	42.7	86.7	13.3	0.87
42.8	13.8	43.4	75.7	24.3	0.76
29.8	25.4	44.9	54.0	46.0	0.54
19.3	34.1	46.7	36.1	63.9	0.36
6.2	46.1	47.6	11.9	88.1	0.12
0.0	51.7	48.3	0.0	100.0	0.00

Table 4.11: Thickness and growth ratio of the fifth batch of samples.

Composition x	Thickness ±5 nm	Growth ratio nm/min
1.00	60	2.0
0.87	75	2.6
0.54	70	2.3
0.12	60	2.0
0.00	80	2.7
0.76	60	2.0
0.36	40	1.3

4.3 Structural analysis

XRD was used to structurally characterize the samples from all batches. As it was mentioned previously, from the first set of samples there were two samples where power was only applied to the Cu target, one with an RF source and one with a DC source; and also two samples with only Zn, following the same configurations. Figure 4.4 shows the results from these four samples, comparing them to the powder diffractograms expected from monoclinic CuO and Wurtzite ZnO. From this figure, we can see that both samples with x = 0.00 have peaks corresponding to the ZnO Wurtzite structure. The very pronounced (002) peak, with a weaker (103), shows high film crystallinity [64]. The peak intensities for the film are, however, very different from those of ZnO powder. This phenomenon has been observed previously and attributed to the preferential orientation of the c-axis normal to the substrate surface [65, 66].

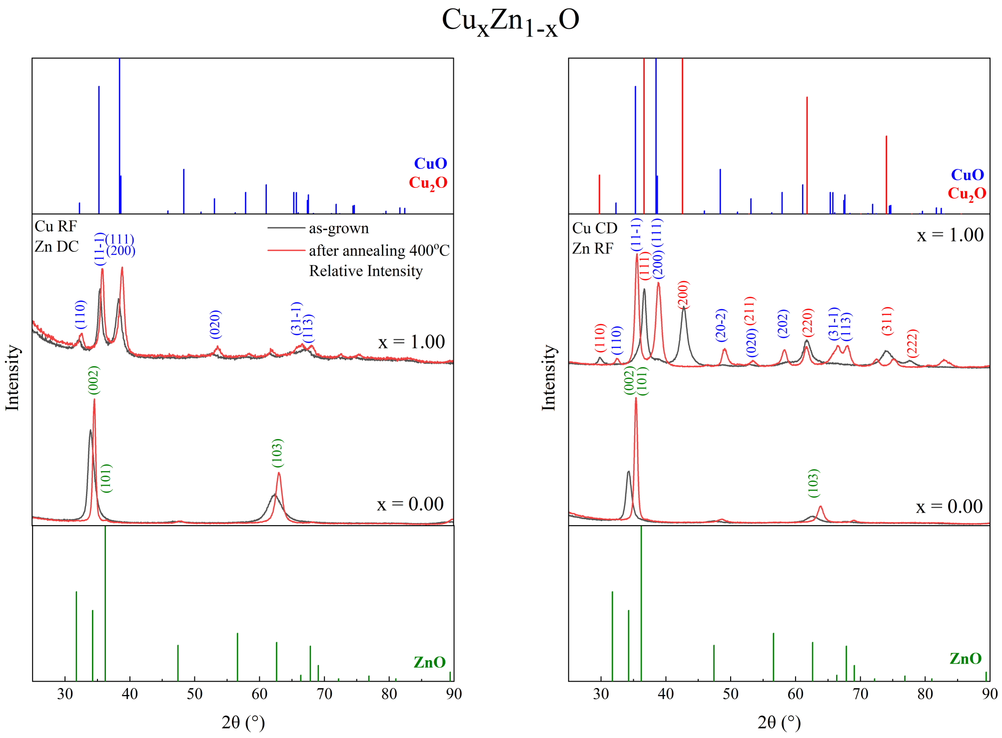

Figure 4.4: XRD of the CuO (x=1.00) and ZnO (x=0.00) samples obtained from the first set of samples, using Zn targets on a DC source and Cu on RF (left), and vice versa (right).

From figure 4.4, we can see that the samples with x = 1.00 show different phases depending on the power source used. The sample deposited with Cu in an RF source shows peaks corresponding to the monoclinic CuO phase, these peaks show higher intensity and definition after undergoing annealing at 400 °C , showing that annealing increased the crystallinity of the sample [67, 68]. On the other hand, the sample deposited with Cu in the DC power source exhibits intense peaks corresponding to the (111), (200), and (311) planes of the cubic Cu_2O phase. However, after annealing the sample, we see that the peaks shifted and now correspond to the monoclinic CuO phase, with higher intensities, showing an increase in the crystallinity of the sample and a preferential orientation on the (11-1) plane [69].

Figure 4.5 shows the XRD results from all the samples from the first batch, as-grown and after the 400 °C annealing. This analysis reveals that samples grown with Cu in an RF source predominantly consist of CuO, while samples with Cu in the DC source display peaks associated with Cu_2O. The discrepancy in the proportion of Cu and O makes the composition of samples with a combination of Zn and Cu unreliable. However, with increased Zn concentration, ZnO peaks remain prominent across both setups, aligning with expectations.

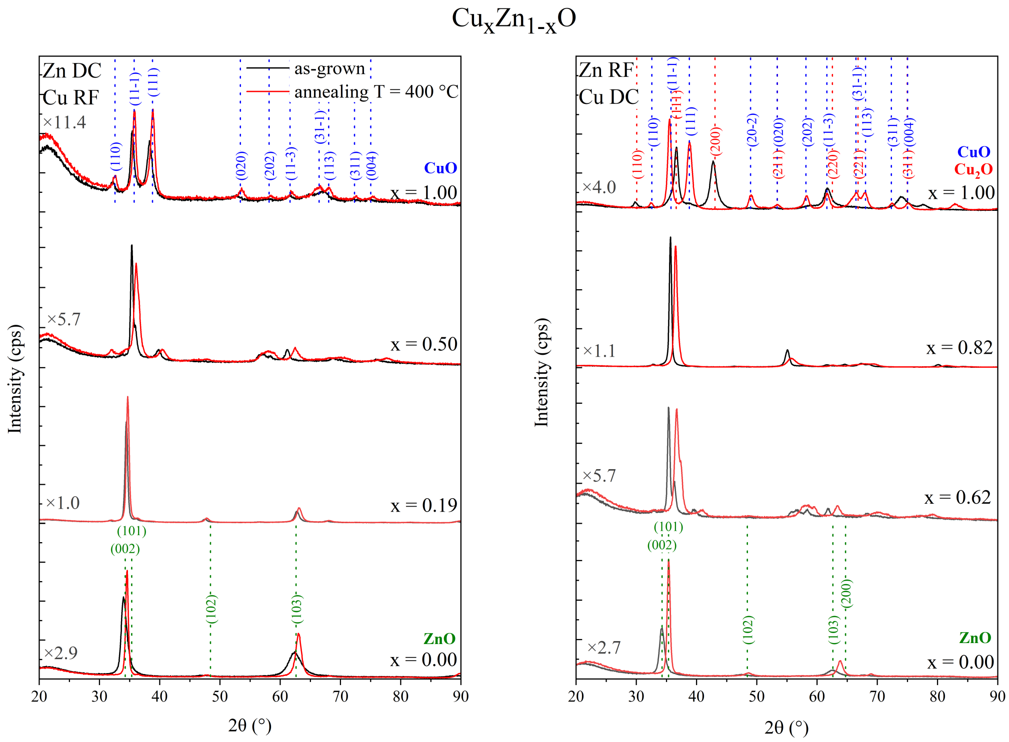

Figure 4.5: XRD results for the first batch of samples, using Zn targets on a DC source and Cu on RF (left), and vice versa (right). Results shown before and after annealing at 400 °C . The x denotes composition as $Cu_xZn_{1-x}O$. Some difractograms were amplified with the given factors for better visual representation.

Figure 4.5 also illustrates the sample's results post-annealing, represented in red. Generally, we observe changes following annealing, with peaks slightly shifting right on the x-axis. Some peaks exhibit a clear increase in crystallite size, indicated by increased height of the peaks and sharpness. Notably, the Cu_2O phase transitions to CuO after annealing, indicating a phase change due to heat treatment.

Additionally, table 4.12 shows some parameters obtained from the fitting, showing that the appearing phases of CuO show a monoclinic structure that corresponds to the space group 15 : C2/c; the Cu_2O phase has a cubic structure corresponding to the space group 224 : Pn-3m; and lastly, the ZnO phase has a Wurtzite hexagonal structure, space group 186 : $P6_3mc$ and this consisten across both setups.

Table 4.12: Lattice parameters obtained for each phase for the CuO, Cu_2O and ZnO for the first batch of samples, together with their corresponding space group.

Phase	a	b	c	α	β	γ	Space Group
Name	Å	Å	Å	o	o	o	
CuO	4.69	3.42	5.13	90.0	99.6	90.0	15 : C2/c
Cu_2O	4.24	4.24	4.24	90.0	90.0	90.0	224 : Pn-3m:2
ZnO	3.25	3.25	5.24	90.0	90.0	120.0	186 : $P6_3mc$

The results, seen in figure 4.6, show the second batch of samples, corresponding to the first trial at the Moorfield PVD. From these samples, the first thing we can see is that the sample with x = 1.00, does not show peaksc corresponding to CuO, which together with the EDS results shown previously, tells us that the material we have is Cu_2O. We conclude that the deposition conditions for the second batch are oxygen-lean, and more oxygen is required during deposition for CuO growth. This set of samples was not further analyzed with UV-vis.

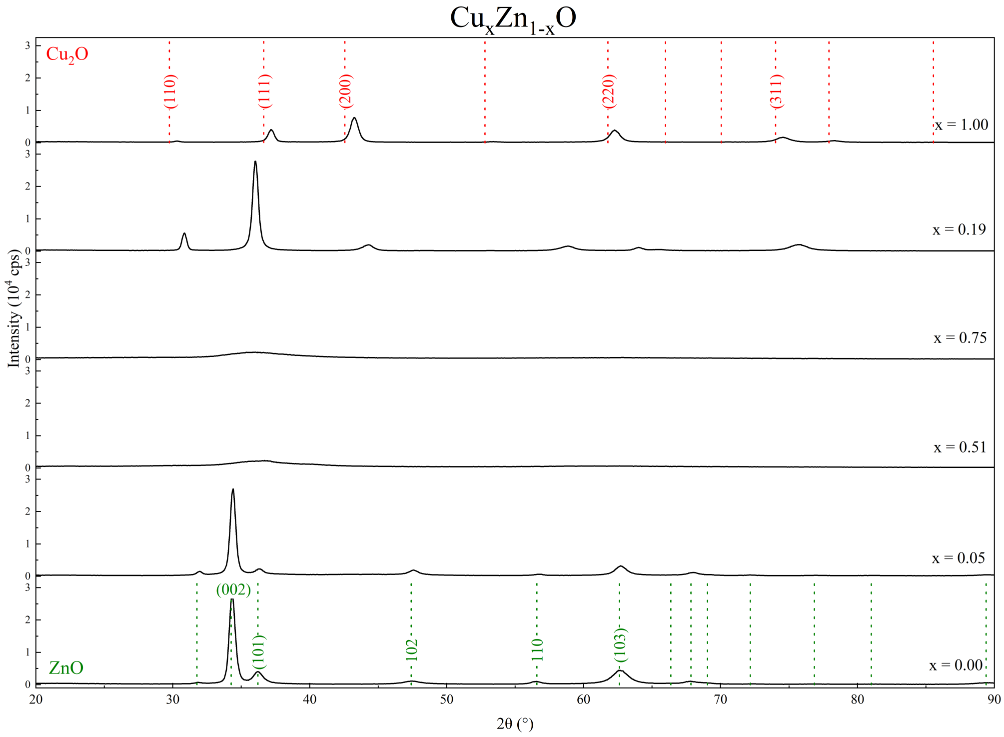

Figure 4.6: XRD results for the second batch of samples, with x denoting the composition.

Lastly, figures 4.7 and 4.8 display the final batches of samples produced at higher oxygen partial pressure and various deposition temperatures (200, 400, and 600 °C). Figure 4.7 shows that in these batches we have successfully synthesized the CuO-phase.

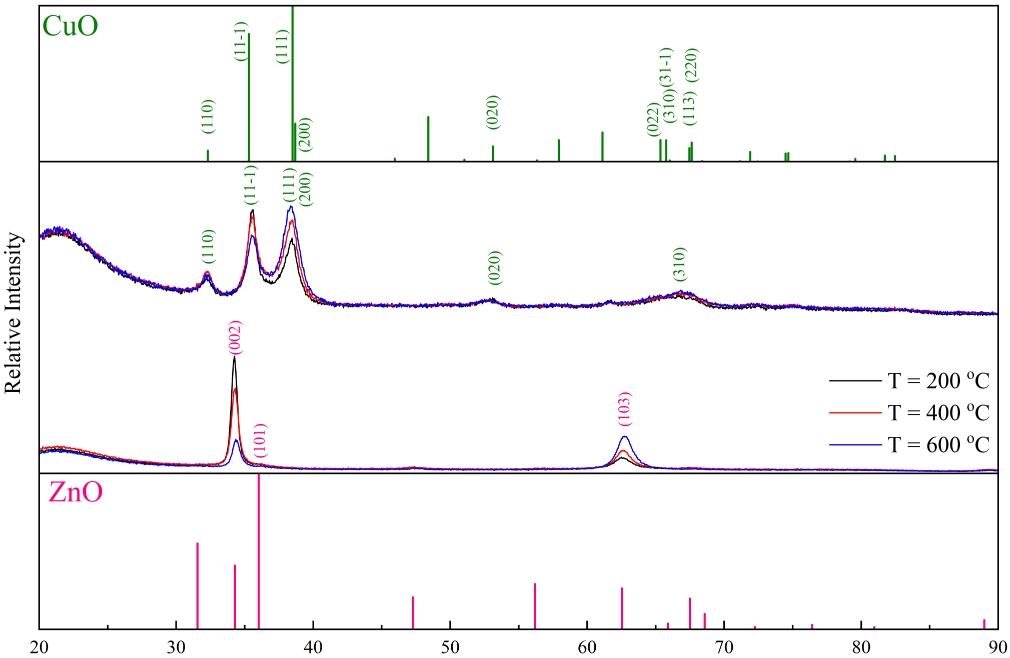

Figure 4.7: XRD powder ZnO and CuO diffractograms compared to the samples with x = 0.00 and x = 1.00 from batches three (T = 200°C), four (T = 400°C) and five (T = 600°C).

The samples of composition x = 1.00 all show the peaks corresponding to the monoclinic CuO structure, but the preferential orientation changes from the (11-1) to the (111) plane as the deposition temperature increases, denoted by the change in height of the corresponding peaks. On the other hand, the samples of composition x = 0.00 exhibit the peaks characteristic of the Zurtzite ZnO, with prominent (002) and (103) peaks, showing high crystallinity. The very high peak (002) shows a c-axis preferential orientation for the samples deposited at 200 and 400 °C , however, the sample deposited at 600 °C shows a preferential orientation towards the (103) plane. Hammad et al. [70] has shown this behaviour to be related to the film thickness for over 240 nm, but considering that the film thickness is 80 nm, this seems to be related to the deposition temperature. In general, these results support EDS measurements and confirm the expected composition and the reproducibility across different deposition temperatures.

Additionally, table 4.13 shows the lattice parameters that were obtained from these graphs for both the CuO (x = 1.00) and ZnO (x = 0.00) samples for each deposition temperature. From this table, we can confirm the right structures that we were expecting, as well as confirming that the deposition method gave consistent samples in structure for the various deposition temperatures.

In addition, examining figure 4.8 illustrates compositional changes, with diminishing CuO peaks transitioning from x = 1.00 to x = 0.45, leading to peak intensity and shape reduction before appearing mostly non-crystalline at x = 0.45. Approaching the

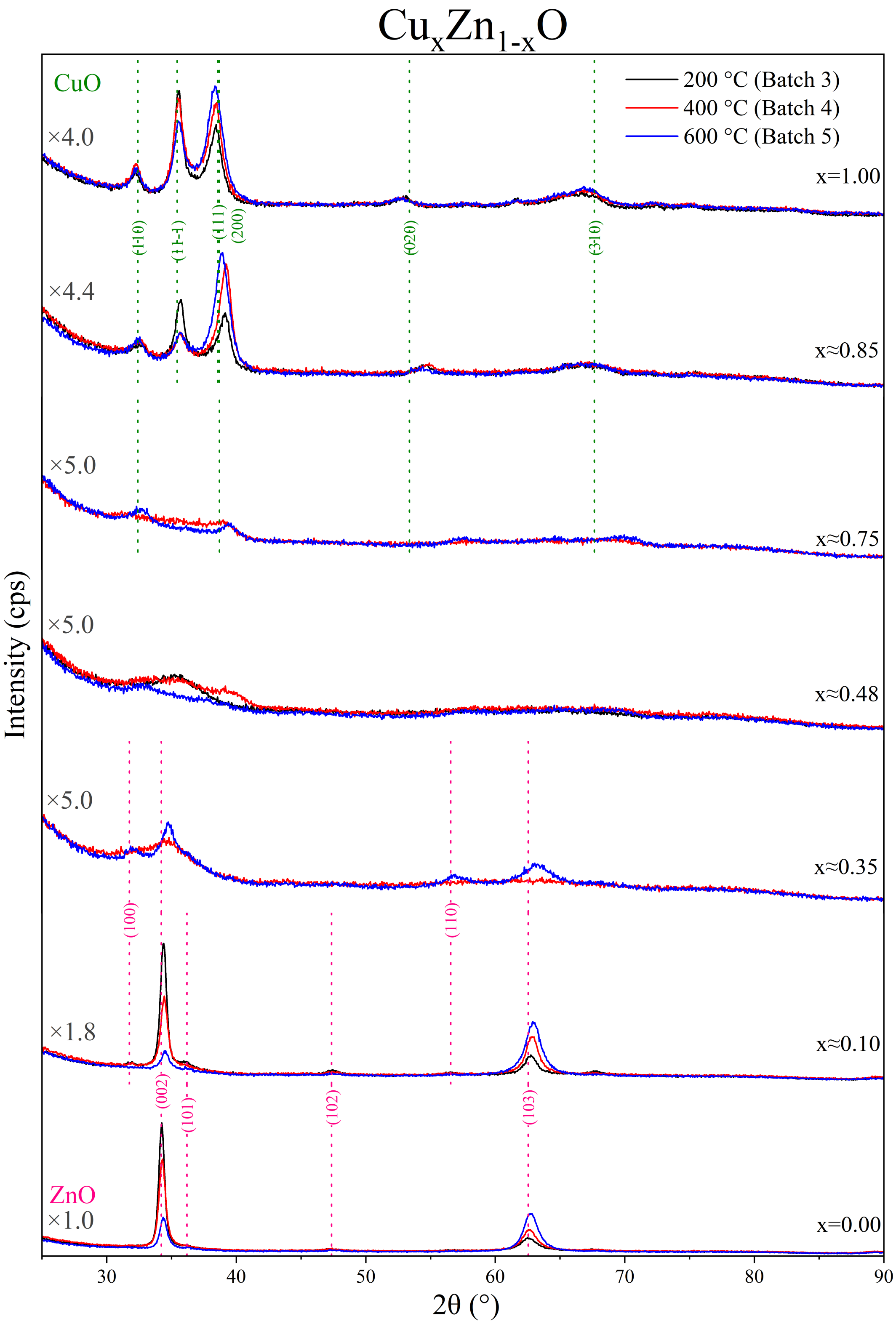

Figure 4.8: XRD results for the last three batches of samples, with varying deposition temperature of T = 200, 400 and 600 °C , with x the composition as $Cu_xZn_{1-x}O$. Some difractograms were amplified with the given factors for better visual representation.

Table 4.13: Lattice Parameters for the CuO (x = 1.00) and ZnO (x = 0.00) samples, obtained from the diffractogram of the last sets of samples and their variations by deposition temperature.

Phase Name	T °C	a Å	b Å	c Å	α ^{o}	β ^{o}	γ ^{o}	Space Group
CuO	200	4.71	3.44	5.16	90.0	99.5	90.0	15 : C2/c
	400	4.70	3.43	5.15	90.0	99.6	90.0	15 : C2/c
	600	4.72	3.45	5.16	90.0	99.5	90.0	15 : C2/c
ZnO	200	3.25	3.25	5.24	90.0	90.0	120.0	186 : P6$_3$mc
	400	3.27	3.27	5.23	90.0	90.0	120.0	186 : P6$_3$mc
	600	3.25	3.25	5.23	90.0	90.0	120.0	186 : P6$_3$mc

ZnO sample (x = 0.00), peaks grow in amplitude, demonstrating alloy effects even as phases predominate in corresponding compositions. Phase disappearance near mid-values suggests a disordered lattice comprising both monoclinic CuO and Wurtzite ZnO phases.

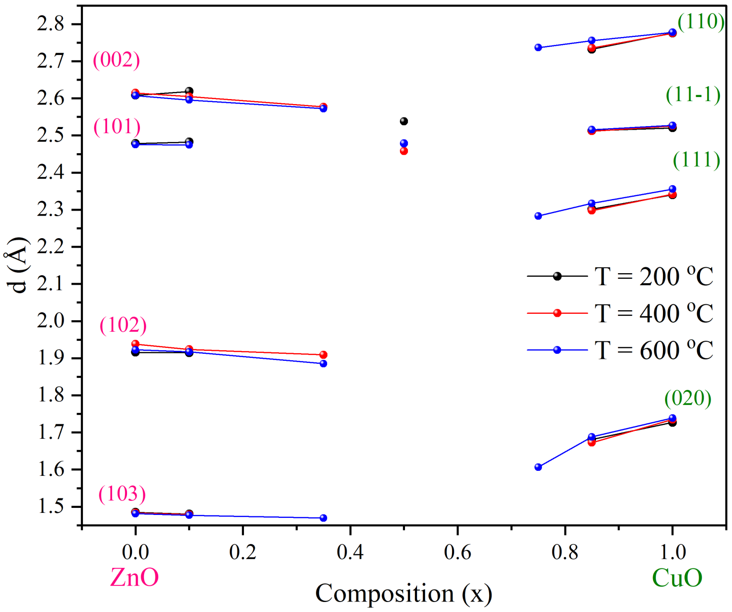

Figure 4.9: Evolution of the distance between planes d with the composition for the planes (002), (101), (102) and (103) of ZnO; and (110), (11-1). (111) and (020) of CuO.

Finally, figure 4.9 highlights peak position changes by assessing interplanar distances d. Distance d generally decreases as we move away from the ZnO composition, evidenced by rightward peak shifts as copper composition increases. Samples with x = 0.45 lack comparable peaks to ZnO (x = 0.00) or CuO (x = 1.00), appearing mostly non-crystalline. Increased copper concentrations subsequently increase d, interpreted as disorder introduction into the lattice by adding zinc atoms, compacting atoms closer together.

4.4 Optical Band-gap Determination

To determine the optical band-gap, we first consider the transmittance and reflectance data gathered using the spectrophotometer. By applying the Beer-Lambert Law, as expressed in equation (3.4), we can derive an expression for the absorption coefficient and plot it in terms of photon energy. To determine the band-gap, we have examined the Tauc plots, which take the form of equation (3.8) for an indirect band-gap and equation (3.9) for a direct band-gap. From these plots, we can estimate the band-gap by identifying the point at which the linear part of the plots intersect the x-axis. Error bars were determined by making various fittings to the linear fit of the graph and averaging the changes to the band gap to the first decimal.

4.4.1 First batch

Now that we understand the procedure, we can analyze figure 4.10 as it displays the transmittance and reflectance data for the first set of samples: figure 4.10a shows the samples as-grown, while 4.10b presents the results after annealing. From these graphs, we observe some disorder in the behavior of the data, with no clear pattern, as samples that were intended to have the same composition, such as x = 1.00, do not exhibit uniform behavior, further confirming the observations made in previous sections. Additionally, since the sample thickness varies significantly among the samples, it becomes increasingly challenging to draw conclusions at this stage.

Furthermore, we can examine the results obtained from the absorption coefficient graphs of these samples, as shown in figures 4.10c and 4.10d. In these figures, we observe that while both samples of ZnO (x = 0.00) behave similarly, as expected, the samples deposited with only Cu exhibit significant variation in their shape and behaviour. For instance, the sample with x = 1.00 when Cu was deposited with an RF power source shows absorption on-set around 1-1.5 eV, which is expected of CuO. In contrast, the sample with x = 1.00 with the Cu target on the DC source, has the on-set around 2-2.5 eV. This can be explained by the XRD results, where this sample was identified as having a Cu_2O and cuprous oxide (Cu_2O) has a known band gap of 2.1 eV.

We can also examine the graphs in figure 4.11, which displays the Tauc plots used to determine the band-gap for this set of samples by using a linear fit in the linear sections of the graph. Furthermore, figure 4.11e illustrates the relationship between the band gap measured for these samples and their composition. Notably, while the ZnO samples (x = 0.00) have very similar band-gaps, the CuO samples vary significantly depending on the deposition process and heat treatment. However, since the growth of the CuO previously demonstrated inconsistencies, we will see shortly that this situation improved in the subsequent batches of samples.

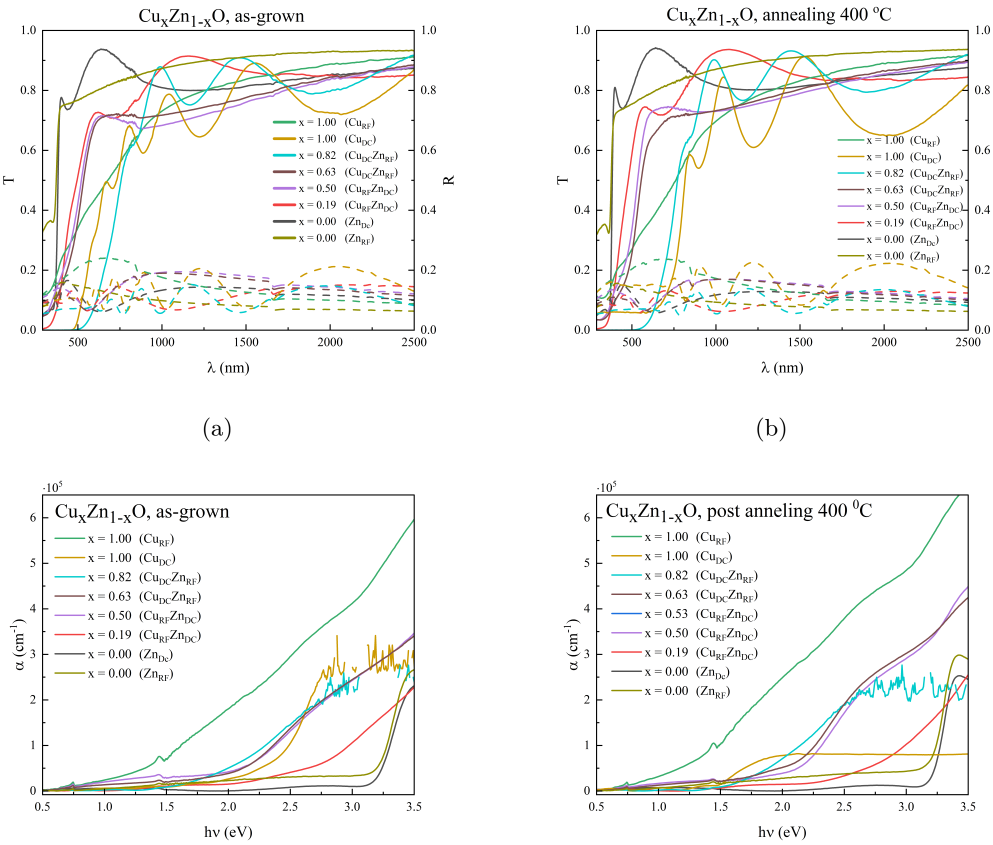

(a) (b)

(c) (d)

Figure 4.10: Transmittance and Reflectance (dotted line) results for the first set of samples, shown as-grown (a) and after annealing (b) at 400 °C . Absorption coefficient obtained for the first set of samples, as-grown (c) and post annealing (d).

4.4.2 Batches three, four and five

Since the second batch of samples did not exhibit the correct phase of CuO, it was not characterized with the spectrophotometer. Instead, we will begin discussing the last three batches of samples.

Figure 4.12 presents the transmittance and reflectance data gathered for the last three sets of samples, highlighting their variations with deposition temperature and composition. One notable observation is that these curves are much more organized compared to those from the first batch. They follow a clear pattern, where the percentage of light transmitted increases as the amount of copper in the sample is reduced. This is expected, as ZnO is nearly transparent and allows most of the spectrum to pass through. Furthermore, in figure 4.12, we can see the sum of both transmittance and reflectance. In the region following the drop in both samples with the highest Zn content, the sum remains around 100%, while the other samples show lower percentages. This discrepancy may be attributed to defects in the samples, which result in a portion of light being absorbed at lower energies (longer wavelengths) for those samples.

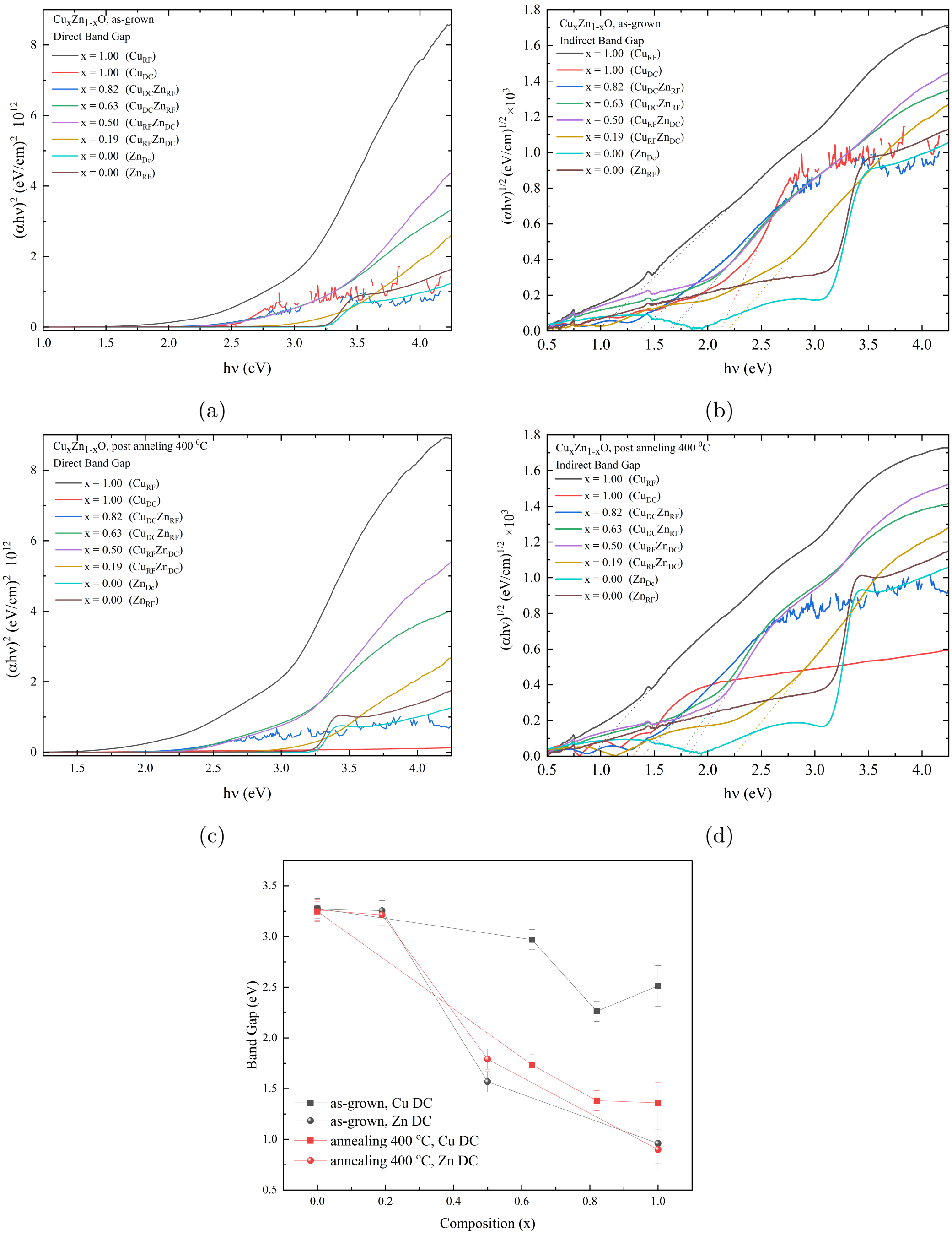

(a) (b)

(c) (d)

(e)

Figure 4.11: Direct and indirect band gap determination for the first batch of samples as-grown and after annealing at 400 °C , using a Tauc plot. Band gap values as a function of composition for the first batch of samples.

Examining the graphs in figure 4.13, we see that the patterns also manifest in the absorption coefficient (α) of the samples. ZnO displays a distinct drop, with a slope that intersects the x-axis at approximately 3.2 eV, as expected for this material. As we increase the copper composition, the slope continues to intersect the x-axis at progressively lower values. Then, we expect a similar behaviour for the band gap values,

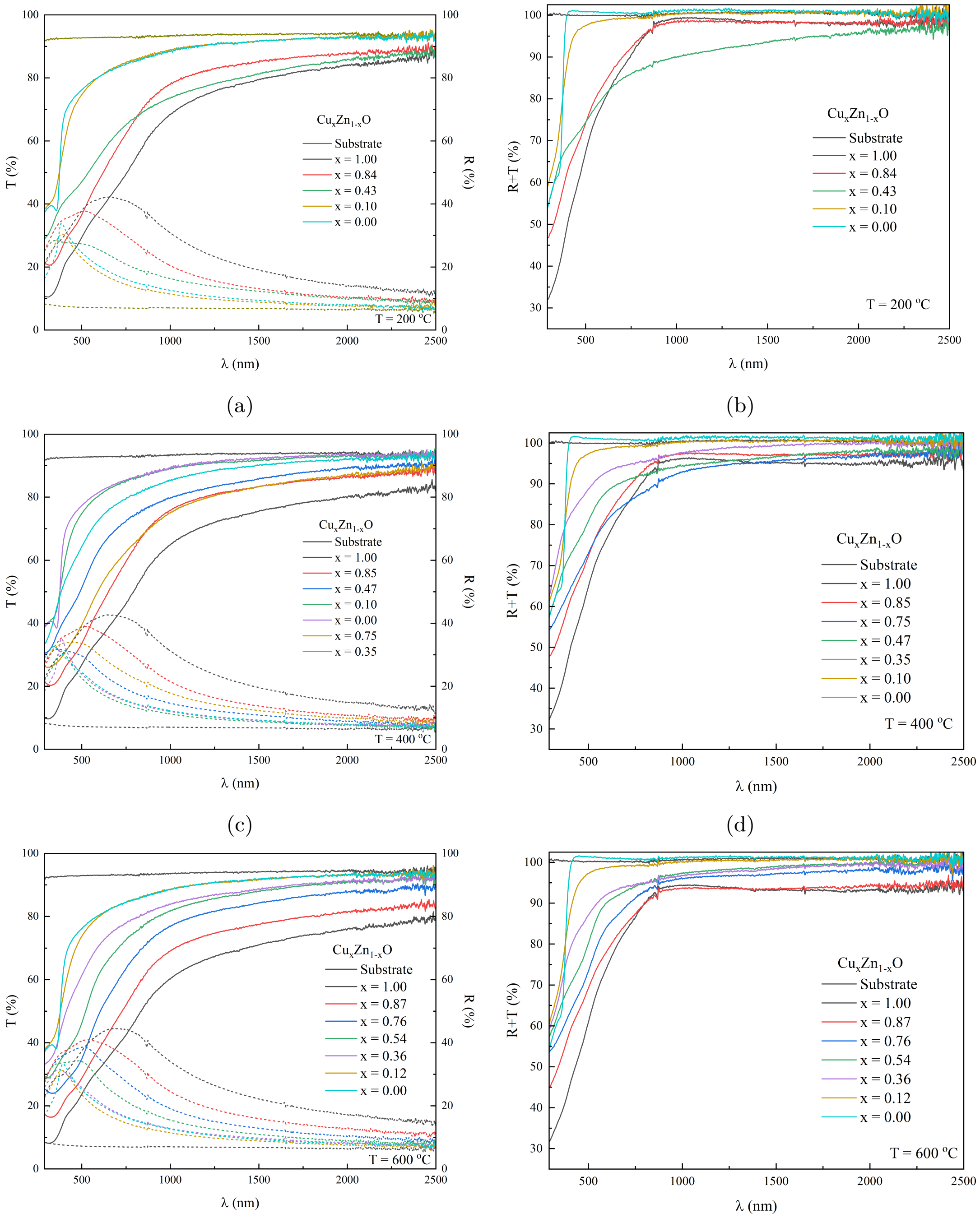

(a) (b)

(c) (d)

(e) (f)

Figure 4.12: Transmittance and Reflectance (dotted line) data, as well as the sums, for the last three sets of samples, for the various deposition temperatures at 200, 400 and 600 °C (top to bottom).

as this signals the energies at which the samples start absorbing the photons.

The graphs shown in figure 4.14 show the Tauc plots that were used in order to determine the direct and indirect band gap of the samples deposited at 200, 400 and 600 °C . While all the samples have very clear linear parts in the direct band gap Tauc plot, only some of them have it for the indirect band gap. However, CuO is known for having

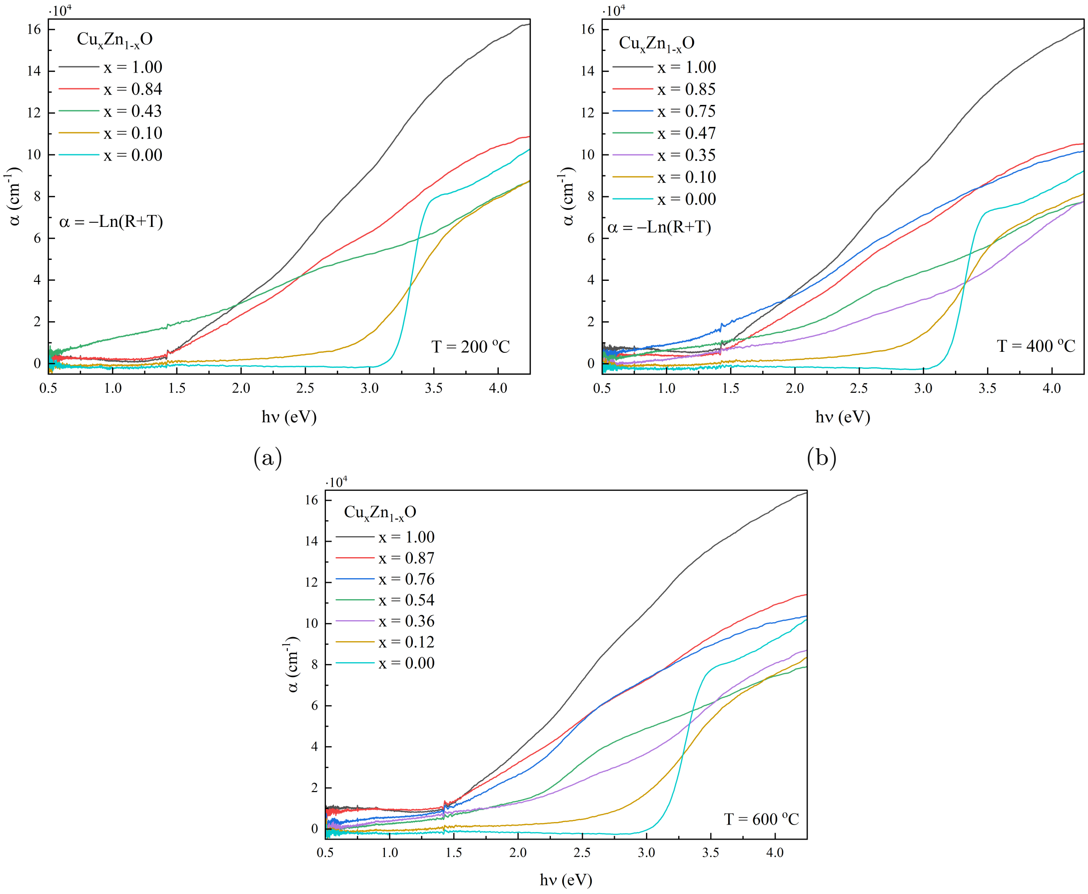

(a) (b)

(c)

Figure 4.13: Absorption coefficient for the last three batches of samples.

an indirect band gap [30], as such we expect the same here. The apparition of a clear value from the direct band gap plots can be explained by considering that for energies considerably bigger than the band gap ($h\nu \gg E_g$) direct transitions are possible, as is exemplified in figure 4.15.

To determine the actual band-gap of each sample, we must consider a few factors: a) CuO has reported an indirect band gap of about 1.1 - 1.4 eV [34, 35], b) ZnO consistently exhibits a direct band gap of approximately 3.4 eV [8, 70], and c) we can make a visual estimation from the absorption coefficient graphs in figure 4.13. By considering these points, we propose that the samples with larger x values, indicating higher copper content, have an indirect band gap, which aligns with the observations made in the absorption coefficient graphs, and that the samples with more zinc in their composition have a direct band gap. Figure 4.16 shows the band structure of CuO and ZnO, with their expected band gaps.

Lastly, we can examine figure 4.17, which illustrate the points discussed. In figure 4.17, we consider that only the samples with a high Zn content relative to Cu have a direct band gap. From this graph, we observe that the transitions are somewhat smoother and appear to be more consistent with the trends seen in the absorption coefficient graphs.

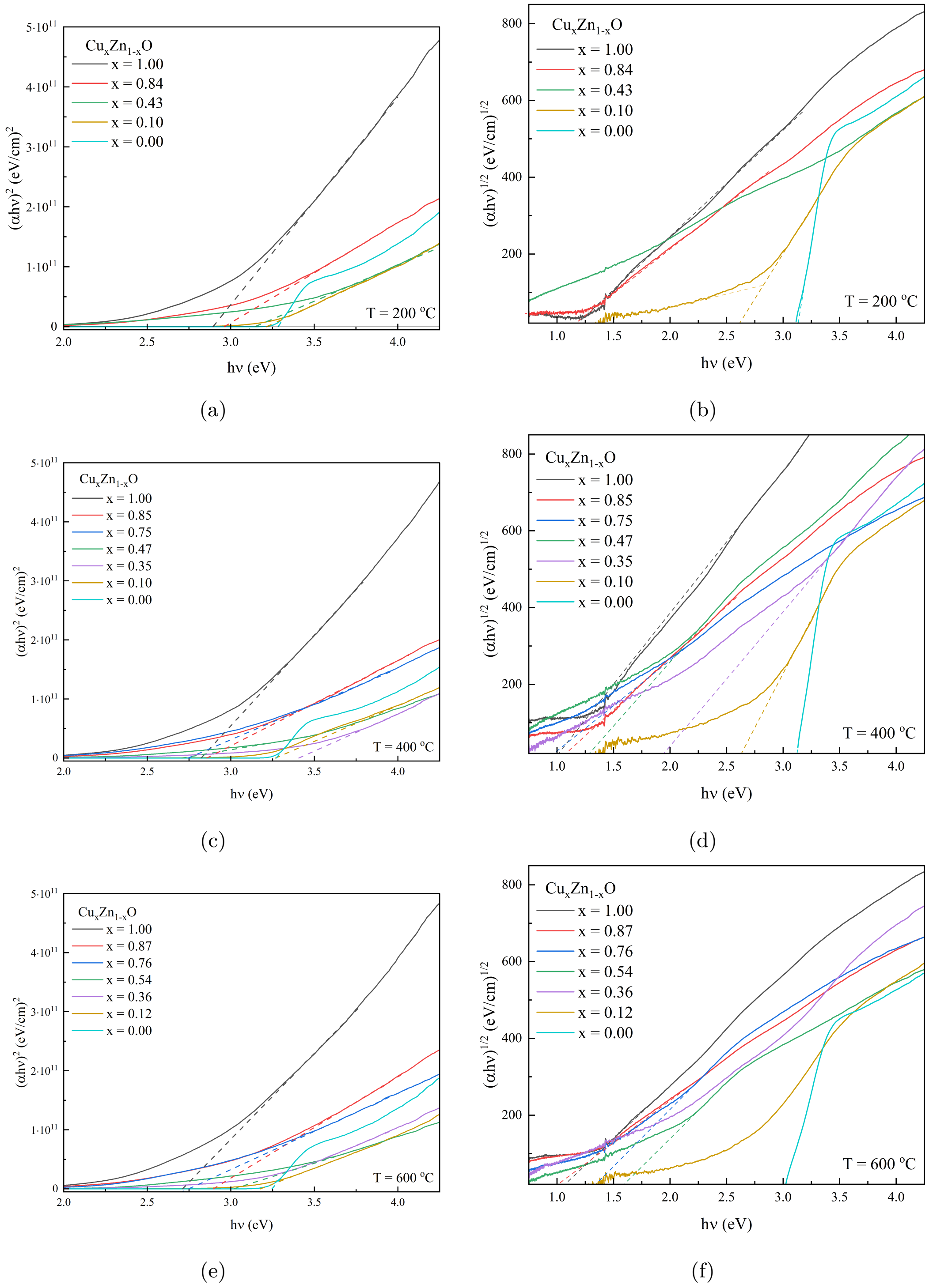

(a)

(b)

(c)

(d)

(e)

(f)

Figure 4.14: Direct (left) and indirect (right) band gap determination for the samples deposited at 200, 400 and 600 °C , using a Tauc plot.

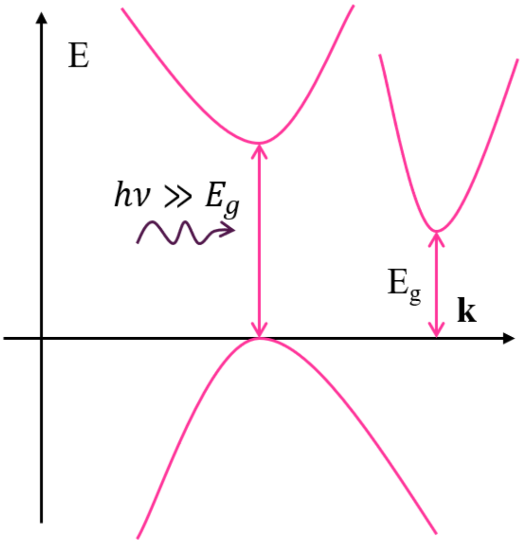

Figure 4.15: Schematic showing direct transition in an indirect semiconductor.

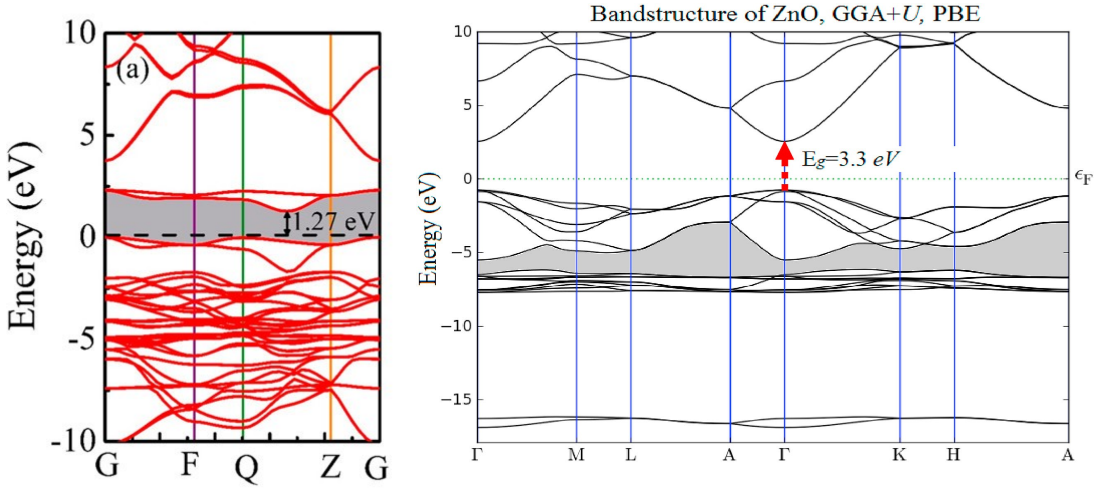

(a)

(b)

Figure 4.16: Band structure of CuO by Yang et al. [7] and ZnO by Jafarova and Orudzhev [8]

Additionally, we see some promising samples with band gaps between 1.5 and 1.9 eV and in the batches corresponding to the higher deposition temperatures and for the compositions between x = 0.35 and x = 0.55. Considering the XRD results, with the increase in crystallinity from these samples by increasing the deposition temperature, and UV-vis results, we can propose that looking into samples with an intermidiate composition might give the expected band gap of 1.7 eV.

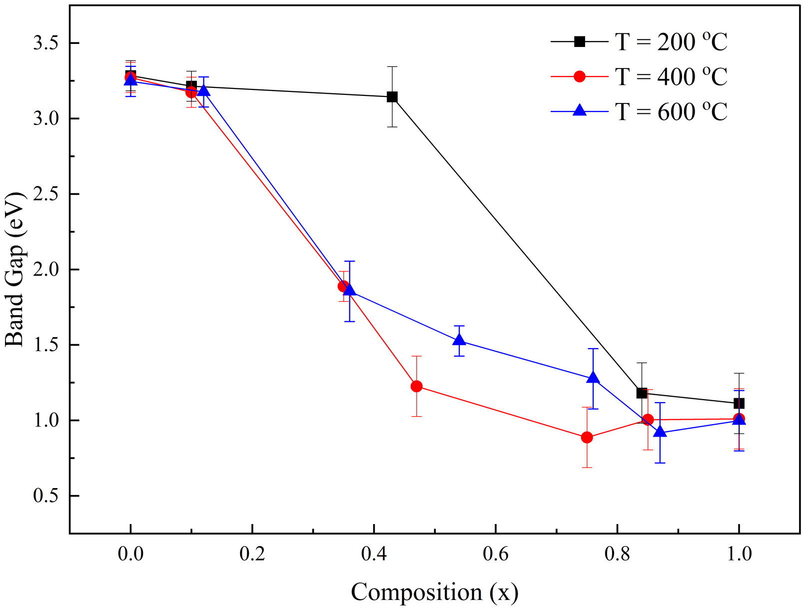

Figure 4.17: Direct band gap as a function of composition.

Chapter 5

Conclusions

The system $Cu_xZn_{1-x}O$ was studied, determining the effect of different deposition parameters and heat treatments on the structural and optical characteristics of the samples. Thus, we can conclude the following:

- The deposition of the samples by reactive magnetron sputtering using RF sources in an Ar:O_2 (10:10 sccm) atmosphere proved to be reliable in obtaining the monoclinic CuO phase when using a Cu target and the Wurtzite hexagonal ZnO structure when using a Zn target. Additionally, the variations in power were shown to be consistent in varying the composition of the samples by the atomic percentage x, with the settings just described.

- XRD showed that the deposition of ZnO on fused silica produces highly crystalline samples, with the preferential orientation dependent on the deposition temperature, and it is not as sensitive to lower oxygen conditions.

  On the other hand, CuO phases required higher oxygen partial pressure to obtain the monoclinic structure, but this came at the cost of lower crystallinity in the samples. Additionally, the preferred orientation of growth changed with the deposition temperature, going from the (11-1) plane at 200 °C to the (111) plane at 600 °C . Furthermore, annealing increased the crystallinity of the $x = 0.00$ and $x = 1.00$ samples but shifted the position of the peaks. In the case of the sample showing a cubic Cu_2O phase, annealing changed it to the monoclinic CuO.

  It was also shown that changes in composition affect the position of the peaks, where the purest phases ($x = 0.00$ and $x = 1.00$) have greater interplanar distances (d) than the mixed samples. Additionally, the samples closer to $x = 0.50$ in composition displayed less crystallinity than the extremes.

- From the UV-vis results, we have observed that the ZnO samples showed almost no absorption for photon energies below the band gap value, shown by the absorption coefficient (α) and the transmittance plus reflectance ($R + T$) graphs. Increasing the amount of Cu in the samples also increased the absorption for energies below the band gap of the samples. This further confirmed observations from XRD that the ZnO samples are highly crystalline while the CuO samples likely have more defects, which increased their absorption and lowered their crystallinity.

Furthermore, it was observed that the band gap can be tuned by varying the composition x according to the system $Cu_xZn_{1-x}O$, making it possible to achieve band gap values close to the ideal 1.7 eV, especially for higher deposition temperatures.

Bibliography

[1] Anubhav Jain et al. ‘Commentary: The Materials Project: A materials genome approach to accelerating materials innovation’. en. In: APL Materials 1.1 (July 2013). Publisher: AIP Publishing. ISSN: 2166-532X. DOI: 10.1063/1.4812323. URL: https://pubs.aip.org/apm/article/1/1/011002/119685/Commentary-The-Materials-Project-A-materials (visited on 01/05/2025).

[2] Materials Data on CuO by Materials Project. en. 2020. DOI: 10.17188/1285757. URL: https://www.osti.gov/servlets/purl/1285757/ (visited on 01/05/2025).

[3] Materials Data on ZnO by Materials Project. en. 2020. DOI: 10.17188/1196748. URL: https://www.osti.gov/servlets/purl/1196748/ (visited on 08/04/2025).

[4] Ben G. Streetman and Sanjay Kumar Banerjee. Solid State Electronic Devices. English. 7. ed., global ed. Always learning. Boston Munich: Pearson, 2016. ISBN: 978-1-292-06055-2.

[5] Sven Rühle. ‘Tabulated values of the Shockley–Queisser limit for single junction solar cells’. In: Solar Energy 130 (June 2016), pp. 139–147. ISSN: 0038-092X. DOI: 10.1016/j.solener.2016.02.015. URL: https://www.sciencedirect.com/science/article/pii/S0038092X16001110 (visited on 15/04/2025).

[6] ‘Physical Vapor Deposition’. en. In: The Materials Science of Semiconductors. Ed. by Angus Rockett. Boston, MA: Springer US, 2008, pp. 505–572. ISBN: 978-0-387-68650-9. DOI: 10.1007/978-0-387-68650-9_11. URL: https://doi.org/10.1007/978-0-387-68650-9_11 (visited on 11/02/2025).

[7] Jiayan Yang et al. ‘Composition Dependence of Optical Properties and Band Structures in p-Type Ni-Doped CuO Films: Spectroscopic Experiment and First-Principles Calculation’. In: The Journal of Physical Chemistry C 123.44 (Nov. 2019). Publisher: American Chemical Society, pp. 27165–27171. ISSN: 1932-7447. DOI: 10.1021/acs.jpcc.9b08604. URL: https://doi.org/10.1021/acs.jpcc.9b08604 (visited on 30/04/2025).

[8] V. N. Jafarova and G. S. Orudzhev. ‘Structural and electronic properties of ZnO: A first-principles density-functional theory study within LDA(GGA) and LDA(GGA)+U methods’. In: Solid State Communications 325 (Feb. 2021), p. 114166. ISSN: 0038-1098. DOI: 10.1016/j.ssc.2020.114166. URL: https:

//www.sciencedirect.com/science/article/pii/S003810982030661X (visited on 07/05/2025).

[9] Atika Qazi et al. ‘Towards Sustainable Energy: A Systematic Review of Renewable Energy Sources, Technologies, and Public Opinions’. In: IEEE Access 7 (2019). Conference Name: IEEE Access, pp. 63837–63851. ISSN: 2169-3536. DOI: 10.1109/ACCESS.2019.2906402. URL: https://ieeexplore.ieee.org/document/8721134 (visited on 15/11/2023).

[10] Mugdha V. Dambhare, Bhavana Butey and S. V. Moharil. ‘Solar photovoltaic technology: A review of different types of solar cells and its future trends’. en. In: Journal of Physics: Conference Series 1913.1 (May 2021). Publisher: IOP Publishing, p. 012053. ISSN: 1742-6596. DOI: 10.1088/1742-6596/1913/1/012053. URL: https://dx.doi.org/10.1088/1742-6596/1913/1/012053 (visited on 31/10/2023).

[11] Jenny Nelson. The physics of solar cells. English. Reprinted. London: Imperial College Press, 2010. ISBN: 978-1-86094-349-2 978-1-86094-340-9.

[12] Romain Cariou et al. ‘III–V-on-silicon solar cells reaching 33% photoconversion efficiency in two-terminal configuration’. en. In: Nature Energy 3.4 (Apr. 2018). Number: 4 Publisher: Nature Publishing Group, pp. 326–333. ISSN: 2058-7546. DOI: 10.1038/s41560-018-0125-0. URL: https://www.nature.com/articles/s41560-018-0125-0 (visited on 21/11/2023).

[13] Xinge Yu, Tobin J. Marks and Antonio Facchetti. ‘Metal oxides for optoelectronic applications’. en. In: Nature Materials 15.4 (Apr. 2016). Number: 4 Publisher: Nature Publishing Group, pp. 383–396. ISSN: 1476-4660. DOI: 10.1038/nmat4599. URL: https://www.nature.com/articles/nmat4599 (visited on 22/11/2023).

[14] Laurentiu Fara et al. ‘Review: Heterojunction Tandem Solar Cells on Si-Based Metal Oxides’. en. In: Energies 16.7 (Jan. 2023). Number: 7 Publisher: Multidisciplinary Digital Publishing Institute, p. 3033. ISSN: 1996-1073. DOI: 10.3390/en16073033. URL: https://www.mdpi.com/1996-1073/16/7/3033 (visited on 22/11/2023).

[15] ‘Edmond Becquerel’. English. In: (Mar. 2016). DOI: 10.1063/PT.5.031182. URL: https://pubs.aip.org/physicstoday/online/8853/Edmond-Becquerel (visited on 25/10/2024).

[16] William Grylls Adams and R. E. Day. ‘V. The action of light on selenium’. In: Proceedings of the Royal Society of London 25.171-178 (Jan. 1997). Publisher: Royal Society, pp. 113–117. DOI: 10.1098/rspl.1876.0024. URL: https://royalsocietypublishing.org/doi/10.1098/rspl.1876.0024 (visited on 08/05/2025).

[17] C. E. Fritts. ‘On a new form of selenium cell, and some electrical discoveries made by its use’. en. In: American Journal of Science s3-26.156 (Dec. 1883). Publisher: American Journal of Science, pp. 465–472. DOI: 10.2475/ajs.s3-26.156.465. URL: https://ajsonline.org/article/65415 (visited on 08/05/2025).

[18] D. M. Chapin, C. S. Fuller and G. L. Pearson. ‘A New Silicon p-n Junction Photocell for Converting Solar Radiation into Electrical Power’. en. In: Journal of Applied Physics 25.5 (May 1954), pp. 676–677. ISSN: 0021-8979, 1089-7550. DOI: 10.1063/1.1721711. URL: https://pubs.aip.org/jap/article/25/5/676/160783/A-New-Silicon-p-n-Junction-Photocell-for (visited on 25/10/2024).

[19] Best Research-Cell Efficiency Chart. en. URL: https://www.nrel.gov/pv/cell-efficiency.html (visited on 21/11/2023).

[20] Piotr Bojek. Solar PV. en-GB. 2025. URL: https://www.iea.org/energy-system/renewables/solar-pv (visited on 10/03/2025).

[21] Zhengshan (Jason) Yu, Mehdi Leilaeioun and Zachary Holman. ‘Selecting tandem partners for silicon solar cells’. en. In: Nature Energy 1.11 (Sept. 2016). Publisher: Nature Publishing Group, pp. 1–4. ISSN: 2058-7546. DOI: 10.1038/nenergy.2016.137. URL: https://www.nature.com/articles/nenergy2016137 (visited on 05/03/2025).

[22] Martin A. Green. ‘Commercial progress and challenges for photovoltaics’. en. In: Nature Energy 1.1 (Jan. 2016). Publisher: Nature Publishing Group, pp. 1–4. ISSN: 2058-7546. DOI: 10.1038/nenergy.2015.15. URL: https://www.nature.com/articles/nenergy201515 (visited on 06/03/2025).

[23] Akihiro Kojima et al. ‘Organometal Halide Perovskites as Visible-Light Sensitizers for Photovoltaic Cells’. In: Journal of the American Chemical Society 131.17 (May 2009). Publisher: American Chemical Society, pp. 6050–6051. ISSN: 0002-7863. DOI: 10.1021/ja809598r. URL: https://doi.org/10.1021/ja809598r (visited on 16/04/2025).

[24] Juan-Pablo Correa-Baena et al. ‘Promises and challenges of perovskite solar cells’. EN. In: Science (Nov. 2017). Publisher: American Association for the Advancement of Science. DOI: 10.1126/science.aam6323. URL: https://www.science.org/doi/10.1126/science.aam6323 (visited on 16/04/2025).

[25] Martin A. Green, Anita Ho-Baillie and Henry J. Snaith. ‘The emergence of perovskite solar cells’. en. In: Nature Photonics 8.7 (July 2014). Publisher: Nature Publishing Group, pp. 506–514. ISSN: 1749-4893. DOI: 10.1038/nphoton.2014.134. URL: https://www.nature.com/articles/nphoton.2014.134 (visited on 16/04/2025).

[26] Gary Hodes and David Cahen. ‘Perovskite cells roll forward’. en. In: Nature Photonics 8.2 (Feb. 2014). Publisher: Nature Publishing Group, pp. 87–88. ISSN: 1749-4893. DOI: 10.1038/nphoton.2014.5. URL: https://www.nature.com/articles/nphoton.2014.5 (visited on 16/04/2025).

[27] Laurentiu Fara et al. ‘On Numerical Modelling and an Experimental Approach to Heterojunction Tandem Solar Cells Based on Si and Cu2O/ZnO—Results and Perspectives’. en. In: Coatings 14.3 (Mar. 2024). Number: 3 Publisher: Multidisciplinary Digital Publishing Institute, p. 244. ISSN: 2079-6412. DOI: 10.3390/coatings14030244. URL: https://www.mdpi.com/2079-6412/14/3/244 (visited on 16/04/2025).

[28] Dian Wang et al. ‘Stability of perovskite solar cells’. In: Solar Energy Materials and Solar Cells 147 (Apr. 2016), pp. 255–275. ISSN: 0927-0248. DOI: 10.1016/j.solmat.2015.12.025. URL: https://www.sciencedirect.com/science/article/pii/S092702481500673X (visited on 16/04/2025).

[29] B. K. Meyer et al. ‘Binary copper oxide semiconductors: From materials towards devices’. en. In: physica status solidi (b) 249.8 (Aug. 2012). Publisher: Wiley, pp. 1487–1509. ISSN: 0370-1972, 1521-3951. DOI: 10.1002/pssb.201248128. URL: https://onlinelibrary.wiley.com/doi/10.1002/pssb.201248128 (visited on 01/05/2025).

[30] Markus Heinemann, Bianca Eifert and Christian Heiliger. ‘Band structure and phase stability of the copper oxides Cu2O, CuO, and Cu4O3’. en. In: Physical Review B 87.11 (Mar. 2013). Publisher: American Physical Society (APS). ISSN: 1098-0121, 1550-235X. DOI: 10.1103/physrevb.87.115111. URL: https://link.aps.org/doi/10.1103/PhysRevB.87.115111 (visited on 01/05/2025).

[31] W. Y. Ching, Yong-Nian Xu and K. W. Wong. ‘Ground-state and optical properties ofCu2O and CuO crystals’. en. In: Physical Review B 40.11 (Oct. 1989). Publisher: American Physical Society (APS), pp. 7684–7695. ISSN: 0163-1829. DOI: 10.1103/physrevb.40.7684. URL: https://link.aps.org/doi/10.1103/PhysRevB.40.7684 (visited on 01/05/2025).

[32] H Kidowaki, T Oku and T Akiyama. ‘Fabrication and characterization of CuO/ZnO solar cells’. In: Journal of Physics: Conference Series 352 (Mar. 2012). Publisher: IOP Publishing, p. 012022. ISSN: 1742-6596. DOI: 10.1088/1742-6596/352/1/012022. URL: https://iopscience.iop.org/article/10.1088/1742-6596/352/1/012022 (visited on 01/05/2025).

[33] C. E. Ekuma et al. ‘Electronic structure and spectra of CuO’. en. In: The European Physical Journal B 87.1 (Jan. 2014). Company: Springer Distributor: Springer Institution: Springer Label: Springer Number: 1 Publisher: Springer Berlin Heidelberg, pp. 1–6. ISSN: 1434-6036. DOI: 10.1140/epjb/e2013-40949-5.

URL: https://link.springer.com/article/10.1140/epjb/e2013-40949-5 (visited on 01/05/2025).

[34] J. Ghijsen et al. 'Electronic structure ofCu2O and CuO'. en. In: Physical Review B 38.16 (Dec. 1988). Publisher: American Physical Society (APS), pp. 11322–11330. ISSN: 0163-1829. DOI: 10.1103/physrevb.38.11322. URL: https://link.aps.org/doi/10.1103/PhysRevB.38.11322 (visited on 01/05/2025).

[35] F. P. Koffyberg and F. A. Benko. 'A photoelectrochemical determination of the position of the conduction and valence band edges of p-type CuO'. en. In: Journal of Applied Physics 53.2 (Feb. 1982). Publisher: AIP Publishing, pp. 1173–1177. ISSN: 0021-8979, 1089-7550. DOI: 10.1063/1.330567. URL: https://pubs.aip.org/jap/article/53/2/1173/10984/A-photoelectrochemical-determination-of-the (visited on 01/05/2025).

[36] Pabitra K. Nayak et al. 'Photovoltaic solar cell technologies: analysing the state of the art'. en. In: Nature Reviews Materials 4.4 (Apr. 2019). Publisher: Nature Publishing Group, pp. 269–285. ISSN: 2058-8437. DOI: 10.1038/s41578-019-0097-0. URL: https://www.nature.com/articles/s41578-019-0097-0 (visited on 22/10/2024).

[37] Sharon Ann Holgate. Understanding solid state physics. eng. Boca Raton London New York: CRC Press, 2010. ISBN: 978-1-4200-1232-3.

[38] Steven M. Girvin and Kun Yang. Modern condensed matter physics. eng. Cambridge New York: Cambridge university press, 2019. ISBN: 978-1-107-13739-4.

[39] Aldo Di Carlo, Enrico Lamanna and Narges Yaghoobi Nia. 'Photovoltaics'. en. In: EPJ Web of Conferences 246 (2020). Publisher: EDP Sciences, p. 00005. ISSN: 2100-014X. DOI: 10.1051/epjconf/202024600005. URL: https://www.epj-conferences.org/articles/epjconf/abs/2020/22/epjconf_lnes2020_00005/epjconf_lnes2020_00005.html (visited on 04/03/2025).

[40] William Shockley and Hans J. Queisser. 'Detailed Balance Limit of Efficiency of p-n Junction Solar Cells'. en. In: Journal of Applied Physics 32.3 (Mar. 1961), pp. 510–519. ISSN: 0021-8979, 1089-7550. DOI: 10.1063/1.1736034. URL: https://pubs.aip.org/jap/article/32/3/510/505950/Detailed-Balance-Limit-of-Efficiency-of-p-n (visited on 15/04/2025).

[41] Young Hee Lee. 'Beyond the Shockley-Queisser limit: Exploring new frontiers in solar energy harvest'. In: Science 383.6686 (Feb. 2024). Publisher: American Association for the Advancement of Science, eado4308. DOI: 10.1126/science.ado4308. URL: https://www.science.org/doi/10.1126/science.ado4308 (visited on 05/05/2025).

[42] Zeinab Shokrollahi, Mina Piralaee and Asghar Asgari. ‘Performance and optimization study of selected 4-terminal tandem solar cells’. en. In: Scientific Reports 14.1 (May 2024). Publisher: Nature Publishing Group, p. 11515. ISSN: 2045-2322. DOI: 10.1038/s41598-024-62085-0. URL: https://www.nature.com/articles/s41598-024-62085-0 (visited on 05/05/2025).

[43] Andresa Baptista et al. ‘Sputtering Physical Vapour Deposition (PVD) Coatings: A Critical Review on Process Improvement and Market Trend Demands’. en. In: Coatings 8.11 (Nov. 2018), p. 402. ISSN: 2079-6412. DOI: 10.3390/coatings8110402. URL: https://www.mdpi.com/2079-6412/8/11/402 (visited on 11/02/2025).

[44] AR Nyaiesh and L Holland. ‘The dependence of deposition rate on power input for dc and rf magnetron sputtering’. In: Vacuum 31.7 (Jan. 1981), pp. 315–317. ISSN: 0042-207X. DOI: 10.1016/S0042-207X(81)80503-9. URL: https://www.sciencedirect.com/science/article/pii/S0042207X81805039 (visited on 14/02/2025).

[45] K. Ellmer and R. Wendt. ‘D.c. and r.f. (reactive) magnetron sputtering of ZnO:Al films from metallic and ceramic targets: a comparative study’. en. In: Surface and Coatings Technology 93.1 (Aug. 1997), pp. 21–26. ISSN: 02578972. DOI: 10.1016/S0257-8972(97)00031-5. URL: https://linkinghub.elsevier.com/retrieve/pii/S0257897297000315 (visited on 15/02/2025).

[46] Matt Hughes. What is DC Sputtering? - Semicore Equipment Inc. en-US. Section: News & Articles. Nov. 2016. URL: https://www.semicore.com/news/94-what-is-dc-sputtering (visited on 15/02/2025).

[47] Milton Ohring. ‘Chapter 5 - Plasma and Ion Beam Processing of Thin Films’. In: Materials Science of Thin Films (Second Edition). Ed. by Milton Ohring. San Diego: Academic Press, Jan. 2002, pp. 203–275. ISBN: 978-0-12-524975-1. DOI: 10.1016/B978-012524975-1/50008-2. URL: https://www.sciencedirect.com/science/article/pii/B9780125249751500082 (visited on 14/02/2025).

[48] Charles Kittel. Introduction to solid state physics. 8th ed. Hoboken, NJ: Wiley, 2005. ISBN: 978-0-471-41526-8.

[49] A. R. Zanatta. ‘Revisiting the optical bandgap of semiconductors and the proposal of a unified methodology to its determination’. In: Scientific Reports 9 (Aug. 2019), p. 11225. ISSN: 2045-2322. DOI: 10.1038/s41598-019-47670-y. URL: https://www.ncbi.nlm.nih.gov/pmc/articles/PMC6677798/ (visited on 28/04/2025).

[50] K Bindu and P K Nair. ‘Semiconducting tin selenide thin films prepared by heating Se–Sn layers’. In: Semiconductor Science and Technology 19.12 (Dec. 2004), pp. 1348–1353. ISSN: 0268-1242, 1361-6641. DOI: 10.1088/0268-1242/19/12/003. URL: https://iopscience.iop.org/article/10.1088/0268-1242/19/12/003 (visited on 20/04/2025).

[51] V. Robles et al. 'Copper tin sulfide (CuxSnSy) thin films evaporated with x = 3,4 atomic ratios: Influence of the substrate temperature and the subsequent annealing in sulfur'. In: Materials Research Bulletin 83 (Nov. 2016), pp. 116–121. ISSN: 0025-5408. DOI: 10.1016/j.materresbull.2016.05.015. URL: https://www.sciencedirect.com/science/article/pii/S0025540816302215 (visited on 20/04/2025).

[52] J. Tauc. 'Optical properties and electronic structure of amorphous Ge and Si'. en. In: Materials Research Bulletin 3.1 (Jan. 1968), pp. 37–46. ISSN: 00255408. DOI: 10.1016/0025-5408(68)90023-8. URL: https://linkinghub.elsevier.com/retrieve/pii/0025540868900238 (visited on 28/04/2025).

[53] Patrycja Makuła, Michał Pacia and Wojciech Macyk. 'How To Correctly Determine the Band Gap Energy of Modified Semiconductor Photocatalysts Based on UV–Vis Spectra'. en. In: The Journal of Physical Chemistry Letters 9.23 (Dec. 2018), pp. 6814–6817. ISSN: 1948-7185, 1948-7185. DOI: 10.1021/acs.jpclett.8b02892. URL: https://pubs.acs.org/doi/10.1021/acs.jpclett.8b02892 (visited on 10/02/2025).

[54] I.G. Hill et al. 'Charge-separation energy in films of -conjugated organic molecules'. en. In: Chemical Physics Letters 327.3-4 (Sept. 2000), pp. 181–188. ISSN: 00092614. DOI: 10.1016/S0009-2614(00)00882-4. URL: https://linkinghub.elsevier.com/retrieve/pii/S0009261400008824 (visited on 06/05/2025).

[55] Dietrich R. T. Zahn, Gianina N. Gavrila and Mihaela Gorgoi. 'The transport gap of organic semiconductors studied using the combination of direct and inverse photoemission'. In: Chemical Physics. Electronic Processes in Organic Solids 325.1 (June 2006), pp. 99–112. ISSN: 0301-0104. DOI: 10.1016/j.chemphys.2006.02.003. URL: https://www.sciencedirect.com/science/article/pii/S0301010406000917 (visited on 06/05/2025).

[56] B. D. Cullity and Stuart R. Stock. Elements of X-ray diffraction. eng. 3. ed. Upper Saddle River, NJ: Prentice Hall, 2001. ISBN: 978-0-201-61091-8.

[57] Osami Sakata and Masashi Nakamura. 'Grazing Incidence X-Ray Diffraction'. en. In: Surface Science Techniques. Springer, Berlin, Heidelberg, 2013, pp. 165–190. ISBN: 978-3-642-34243-1. DOI: 10.1007/978-3-642-34243-1_6. URL: https://link.springer.com/chapter/10.1007/978-3-642-34243-1_6 (visited on 03/05/2025).

[58] Microscopía electrónica de barrido (SEM), ¿para qué me sirve? | Atria. es-ES. Aug. 2020. URL: https://www.atriainnovation.com/microscopia-electronica-de-barrido-sem-utilidades/ (visited on 25/06/2022).

[59] Nicolle Tello Díaz. 'Caracterización estructural e hiperfina del acero Fe-20Mn-0,8C'. spa. Bachelor. Cali, Colombia: Universidad del Valle, 2022. URL: https://bibliotecadigital.univalle.edu.co/entities/publication/f7854f0d-70b5-459f-b69c-190b9aa937b9 (visited on 13/02/2025).

[60] Brent Fultz and James Howe. Transmission Electron Microscopy and Diffractometry of Materials. en. Graduate Texts in Physics. Berlin, Heidelberg: Springer Berlin Heidelberg, 2013. ISBN: 978-3-642-29760-1 978-3-642-29761-8. DOI: 10.1007/978-3-642-29761-8. URL: https://link.springer.com/10.1007/978-3-642-29761-8 (visited on 10/03/2025).

[61] MyScope - Train for advanced research. en. URL: https://myscope.training/ (visited on 10/03/2025).

[62] Vasile-Dan Hodoroaba. 'Chapter 4.4 - Energy-dispersive X-ray spectroscopy (EDS)'. In: Characterization of Nanoparticles. Ed. by Vasile-Dan Hodoroaba, Wolfgang E. S. Unger and Alexander G. Shard. Micro and Nano Technologies. Elsevier, Jan. 2020, pp. 397–417. ISBN: 978-0-12-814182-3. DOI: 10.1016/B978-0-12-814182-3.00021-3. URL: https://www.sciencedirect.com/science/article/pii/B9780128141823000213 (visited on 03/05/2025).

[63] Daisuke Shindo and Tetsuo Oikawa. 'Energy Dispersive X-ray Spectroscopy'. en. In: Analytical Electron Microscopy for Materials Science. Springer, Tokyo, 2002, pp. 81–102. ISBN: 978-4-431-66988-3. DOI: 10.1007/978-4-431-66988-3_4. URL: https://link.springer.com/chapter/10.1007/978-4-431-66988-3_4 (visited on 03/05/2025).

[64] Simona Tuckute et al. 'Structure and Photocatalytic Activity of Copper and Carbon-Doped Metallic Zn Phase-Rich ZnO Oxide Films'. en. In: Catalysts 12.1 (Jan. 2022). Number: 1 Publisher: Multidisciplinary Digital Publishing Institute, p. 60. ISSN: 2073-4344. DOI: 10.3390/catal12010060. URL: https://www.mdpi.com/2073-4344/12/1/60 (visited on 06/05/2025).

[65] E. Restrepo-Parra, L.E. Moreno-Montoya and P.J. Arango-Arango. 'ZnO thin films growth by pulsed vacuum arc discharge'. en. In: Surface and Coatings Technology 204.3 (Oct. 2009), pp. 271–276. ISSN: 02578972. DOI: 10.1016/j.surfcoat.2009.07.020. URL: https://linkinghub.elsevier.com/retrieve/pii/S025789720900588X (visited on 06/05/2025).

[66] Hirofumi Takikawa et al. 'ZnO film formation using a steered and shielded reactive vacuum arc deposition'. In: Thin Solid Films. International Conference on Metallurgic Coatings and Thin Films 377-378 (Dec. 2000), pp. 74–80. ISSN: 0040-6090. DOI: 10.1016/S0040-6090(00)01387-0. URL: https://www.sciencedirect.com/science/article/pii/S0040609000013870 (visited on 06/05/2025).

[67] Funda Aksoy Akgul et al. 'Influence of thermal annealing on microstructural, morphological, optical properties and surface electronic structure of copper oxide thin films'. In: Materials Chemistry and Physics 147.3 (Oct. 2014), pp. 987–995. ISSN: 0254-0584. DOI: 10.1016/j.matchemphys.2014.06.047. URL: https://www.sciencedirect.com/science/article/pii/S0254058414003988 (visited on 07/05/2025).

[68] Oleksii Diachenko et al. ‘Structural and Optical Properties of CuO Thin Films Synthesized Using Spray Pyrolysis Method’. en. In: Coatings 11.11 (Nov. 2021). Number: 11 Publisher: Multidisciplinary Digital Publishing Institute, p. 1392. ISSN: 2079-6412. DOI: 10.3390/coatings11111392. URL: https://www.mdpi.com/2079-6412/11/11/1392 (visited on 07/05/2025).

[69] Arnaud Krumpmann and Rony Snyders. ‘Study of synthesis strategies to improve the electrical properties of magnetron sputtered copper oxide thin films’. In: Journal of Vacuum Science & Technology A 40.1 (Dec. 2021), p. 013412. ISSN: 0734-2101. DOI: 10.1116/6.0001423. URL: https://doi.org/10.1116/6.0001423 (visited on 07/05/2025).

[70] Ahmed H. Hammad et al. ‘Structural and optical properties of ZnO thin films prepared by RF sputtering at different thicknesses’. In: Physica B: Condensed Matter 540 (July 2018), pp. 1–8. ISSN: 0921-4526. DOI: 10.1016/j.physb.2018.04.017. URL: https://www.sciencedirect.com/science/article/pii/S0921452618302813 (visited on 07/05/2025).